nature communications

Article

https://doi.org/10.1038/s41467-025-65449-w

An antimicrobial peptide as a potential therapy for bacterial pneumonia that alleviates antimicrobial resistance

Received: 7 February 2025

Accepted: 15 October 2025

Published online: 25 November 2025

Check for updates

Chao Zhong[1,4], Yongtao He[1,4], Jing Zou[1], Luyang Gao[1], Jiahui Wang[1], Jingyi Zhu[1], Wenjing Xue[1], Sanhu Gou[1], Yun Zhang[1], Hui Liu[1] & Jingman Ni[1,2,3]

Bacterial pneumonia remains a global health threat that is worsened by drug-resistant bacteria, underscoring the need for the development of new antimicrobial agents. Antimicrobial peptides are promising new candidates with broad-spectrum activity and low potential for resistance development. Here, we report a linear antimicrobial peptide (AMP) that consists of four repeating units of (D-tryptophan)-(D-arginine)-(D-lysine). This peptide exhibits high stability and robust antimicrobial activity against multidrug-resistant bacteria, such as methicillin-resistant *Staphylococcus aureus* and *Klebsiella pneumoniae*, and improved biocompatibility. Furthermore, the AMP shows low potential for resistance development and the ability to alleviate resistance and restore antibiotic sensitivity due to multiple mechanisms, including membrane targeting and non-membrane lysis (DNA binding, reactive oxygen species accumulation, ATP depletion, metabolic interference). In vivo, the peptide showed promising therapeutic efficacy in a model of methicillin-resistant *Staphylococcus aureus* and *K. pneumoniae* pneumonia, as well as in a lipopolysaccharide-induced lung injury model.

Pneumonia is a prevalent respiratory disease with high clinical incidence, primarily attributable to various pathogenic factors, with bacterial infections representing the predominant cause[1]. Bacterial pneumonia is manifested through symptoms such as fever, cough, and respiratory difficulties. In the absence of appropriate treatment, these symptoms may result in the impairment of pulmonary function and a disruption in the immune system, which can lead to elevated mortality rates and constitute a considerable public health concern[2]. Among the multitude of pathogens, *Staphylococcus aureus* (*S. aureus*) and *Klebsiella pneumoniae* (*K. pneumoniae*) pose significant challenges in clinical anti-infective treatment due to their high pathogenicity and the emergence of drug resistance.

S. aureus is an important pathogen responsible for bacterial pneumonia, which is usually accompanied by a high mortality rate ranging from 48 to 84%[3]. *S. aureus* secretes various virulence factors, leading to innate immune cell death and complement activation disorder. As the infection progresses, the bacteria aggregate to form biofilms and impede antibiotic and nutrient penetration. Once biofilm is established, *S. aureus* emerges 10–1000 times more resistant to antibiotics than planktonic bacteria[4]. Additionally, *S. aureus* possesses intrinsic resistance mechanisms, including reducing membrane permeability, activating drug efflux systems, and producing excessive β-lactamases[5]. The clinical detection rate of methicillin-resistant *S. aureus* (*MRSA*) is increasing annually, accounting for 60–80% of all *S. aureus* infections. According to monitoring data from the United States, 78% of hospitalized cases with *S. aureus* pneumonia are attributed to *MRSA*, underscoring its status as a critical target for antimicrobial resistance monitoring[6]. While vancomycin has been pivotal

[1]Institute of Pharmaceutics, School of Pharmacy, Key Laboratory of Preclinical Study for New Drugs of Gansu Province, School of Basic Medical Sciences, and Research Unit of Peptide Science, Chinese Academy of Medical Sciences, 2019RU066, Lanzhou University, Lanzhou, PR China. [2]State Key Laboratory of Bioactive Molecules and Druggability Assessment, Jinan University, Guangzhou, PR China. [3]State Key Laboratory of Quality Research in Chinese Medicine, Macau University of Science and Technology, Macao, China. [4]These authors contributed equally: Chao Zhong, Yongtao He. e-mail: nijm@lzu.edu.cn

in treating *MRSA* infections, the ongoing emergence of vancomycin-resistant *S. aureus* presents a serious challenge, highlighting the urgent need for alternative therapeutic strategies[7].

K. pneumoniae, as a representative of gram-negative bacteria, has been classified as an "emergency threat" pathogen by the World Health Organization (WHO)[8]. It can develop into an invasive infection through upper respiratory colonization, particularly in instances of host immune suppression or microbial imbalance, potentially leading to severe pneumonia[9]. While classical *K. pneumoniae* typically exhibits low virulence and coexists with the host without causing significant diseases, immune function or microbial community balance disruptions can transform it into a pathogenic strain capable of causing pneumonia[10]. In recent years, the frequent emergence of hypervirulent *K. pneumoniae* has caused invasive infections, signaling the onset of a new and escalating global public health crisis[8,11]. Concurrently, the prevalence of multidrug-resistant hypervirulent *K. pneumoniae* has escalated, with carbapenem-resistant *K. pneumoniae* emerging as a severe challenge for clinical anti-infective treatment[8]. This strain has been designated as the highest priority pathogen by the WHO[12]. According to the latest WHO global antimicrobial resistance surveillance data, carbapenem-resistant *K. pneumoniae* has been detected in every WHO region globally, with specific areas reporting resistance rates exceeding 50%[13]. As reported by the China Antimicrobial Surveillance Network (CHINET) surveillance on bacterial resistance monitoring, the resistance rate of *K. pneumoniae* to imipenem and meropenem has surged from 3% in 2005 to over 26% in 2022[14]. Additionally, the existing research results also indicate that the mortality of carbapenem-resistant *K. pneumoniae* infection was significantly higher than that of carbapenem-sensitive *K. pneumoniae*, as well as the incidence rate and mortality of patients with carbapenem-resistant *K. pneumoniae* infection in intensive care unit (ICU) settings, surpassing those in non-ICU patients[15].

Antimicrobial peptides (AMPs), also known as host defense peptides, are active ingredients in various organisms, including animals, insects, plants and microorganisms[16]. They have broad-spectrum antimicrobial activity against bacteria, viruses, fungi, and parasites, and some also possess immunomodulatory properties[17]. Unlike small molecules (typically <500 Da), AMPs generally comprise 10–50 amino acids, most of which are positively charged and hydrophobic[16]. The positive charge facilitates the targeting of anionic bacterial membranes via electrostatic attraction, while the hydrophobic regions promote integration into the lipid bilayer, increasing membrane permeability and causing irreversible damage[18,19]. Unlike antibiotics, which typically target a single molecular mechanism, AMPs employ non-receptor-mediated membrane effects. They are efficient antimicrobials against drug-resistant bacteria and are less likely to induce bacterial resistance[18]. In addition, the surface of bacterial membranes is rich in anionic phospholipids and lipopolysaccharides, whereas mammalian cell membranes predominantly contain a large amount of zwitterionic cholesterol and sphingomyelin. Consequently, cationic AMPs preferentially interact with bacterial membranes, sparing host cells. Furthermore, AMPs undergo conformational changes upon contact with bacterial membranes, a property not easily replicated on mammalian cell membranes, contributing to their low cytotoxicity[20]. AMPs lay a solid foundation for developing a new generation of antimicrobial agents.

Despite the predictable therapeutic potential of AMPs, their clinical application still faces a fundamental challenge: their inherent cytotoxicity toward mammalian cells due to non-selective membrane interactions. For example, melittin exerted broad-spectrum antimicrobial activity, but its application is limited due to its significant cytotoxicity to mammalian cells[21]. Although polymyxin B is highly effective against gram-negative bacteria, its nephrotoxicity and neurotoxicity severely narrow its safe treatment window[22]. Recently, optimization strategies for AMPs have mainly focused on structural modifications of natural AMPs (such as cyclization[23], amino acid mutation[24] and lipidation[25]) and innovative design of sequences[26,27]. What is lacking is that the AMPs sequences used for optimization in the study were mostly from natural sources and showed high homology with host defense peptides, which may disrupt the body's innate immune system if tolerance occurred. Consequently, balancing antimicrobial potential with enhanced selectivity through rational design represents a critical challenge that urgently warrants addressing within AMPs design[28].

The cationic nature of AMPs primarily arises from protonated basic amino acids, particularly arginine (pI = 10.76) and lysine (pI = 9.74), which maintain positive charges under physiological conditions. Arginine has a distinctive structural advantage due to its guanidinium side chain. This unique functional group demonstrates exceptional hydrogen bonding capability with phosphate groups in the phospholipid headgroups of bacterial membranes, significantly enhancing AMPs-membrane interactions and contributing to superior antimicrobial efficacy[29,30]. Nonpolar amino acids and specialized hydrophobic motifs predominantly mediate the hydrophobic character of AMPs. Among these, tryptophan is critical due to its indole ring structure. This planar aromatic system facilitates specific interfacial binding with bacterial membranes through π-electron interactions and hydrophobic forces, enabling deeper penetration into the lipid bilayer core. The synergistic combination of these cationic and hydrophobic elements enables AMPs to achieve selective membrane disruption while maintaining structural stability during target engagement[29,31]. With these considerations in mind, in our previous studies, we dedicated significant efforts to synthesizing a series of novel AMPs. Among these, (WRK)4 (WRKWRKWRKWRK-NH_2) emerged as a standout candidate due to its potent antimicrobial activity and high selectivity, both in vitro and in vivo[32]. Most notably, (WRK)4 exerted ideal antimicrobial activity against *MRSA* and *K. pneumoniae*, inspiring us to further explore its potential application as a treatment for bacterial pneumonia. However, (WRK)4 presented a critical limitation: its L-amino acid composition was easily degraded by trypsin and chymotrypsin[33].

In this work, we develop a linear broad-spectrum AMP 1003 carrying four repeating units of (D-tryptophan)-(D-arginine)-(D-lysine) with enhanced stability, robust antimicrobial activity and low toxicity. We systematically evaluate the antimicrobial activity of AMP 1003 both in vitro and in vivo, focusing on its efficacy against *MRSA* and *K. pneumoniae*. We also explore its therapeutic potential for combating bacterial pneumonia, providing a promising foundation for the clinical development of stable and effective AMPs.

Results

Design, synthesis and characterization of AMP 1003

The enzymatic instability of natural AMPs severely restricts their clinical application, and this limitation is particularly prominent in (WRK)4 with a repeating sequence of tryptophan-arginine-lysine developed by our team earlier[32]. It demonstrated notable antimicrobial potential, whereas the composition of L-amino acid rendered it susceptible to protease degradation. To overcome this limitation, we synthesized a linear broad-spectrum AMP 1003 carrying four repeating units of (D-tryptophan)-(D-arginine)-(D-lysine) employing the standard Fmoc solid-phase synthesis strategy (Fig. 1a and Supplementary Fig. 1), and then purified through reverse phase high-performance liquid chromatography (RP-HPLC) (purity = 100%, T_R = 9.577 min) (Supplementary Fig. 2a). The measured molecular weight was confirmed by mass spectrometry and aligned with the theoretical value (Supplementary Fig. 2b), validating successful synthesis.

AMPs generate electrostatic interactions with anionic bacterial membranes under positive charges and insert into the interior of bacterial membranes depending on hydrophobicity, subsequently disrupting the integrity of bacterial membranes and exerting antimicrobial effects[19]. Based on the theoretical prediction of ChemDraw

https://doi.org/10.1038/s41467-025-65449-w

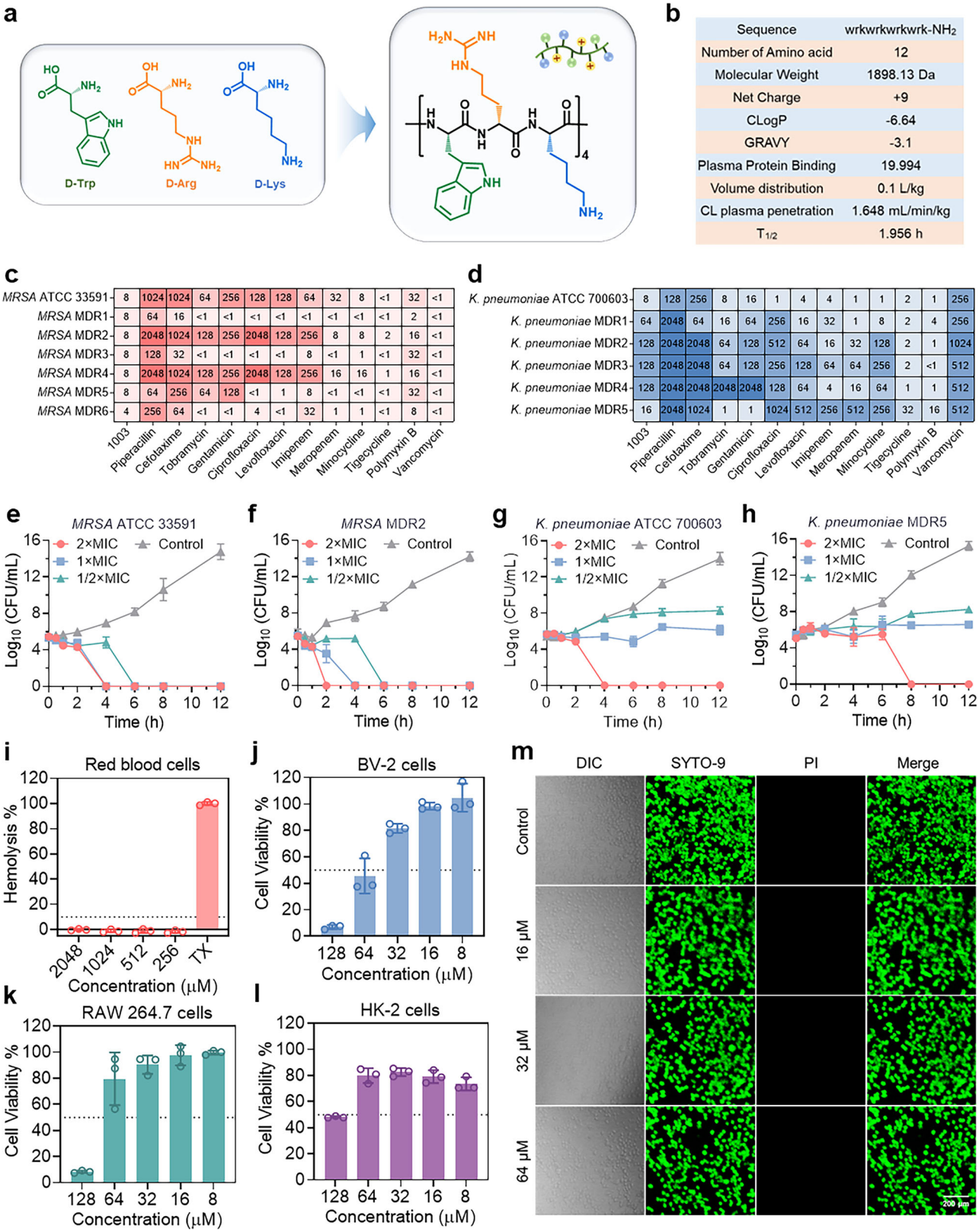

18.0 and ADMET3.0, AMP 1003 presented a net charge of +9 in pH 7.4 and low hydrophobicity (CLogP = −6.64 and GRAVY = −3.1) attributed to the enrichment of D-arginine and D-lysine, which supported its good water solubility (LogS = −2.447). Additionally, the peptide retained a low plasma protein binding rate (19.994%), moderate volume distribution (0.1 L/kg), controllable clearance rate (CL-plasma penetration = 1.648 mL/min/kg), and a reasonable half-life of drugs (1.956 h), indicating its good in vivo delivery potential (Fig. 1b). Meanwhile, the secondary structure of AMP 1003 was analyzed by circular dichroism (CD) spectra, which presented unordered structure either H_2O or 50% TFE (membrane-mimetic environments) (Supplementary Fig. 3). While modulation of secondary structure can fine-tune the antimicrobial activity and toxicity profiles of AMPs (e.g., α-helix stabilization often enhances membrane penetration), well-defined

Fig. 1 | Design of AMP 1003 with an excellent in vitro antimicrobial profile. **a** Chemical structure of AMP 1003. **b** Sequences and key physicochemical parameters of AMP 1003 generated by ChemDraw 18.0 and ADMETlab 3.0. **c**, **d** Antimicrobial activity of AMP 1003 against standard and clinical isolates of multidrug-resistant *MRSA* or *K. pneumoniae*, represented by minimum inhibitory concentration (MIC (μM)). Bacterial killing kinetics of AMP 1003 against *MRSA* ATCC 33591 (**e**), *MRSA* MDR2 (**f**), *K. pneumoniae* ATCC 700603 (**g**) and *K. pneumoniae* MDR5 (**h**), $n = 3$ independent replicates. Data are presented as mean values ± SD. Data points show the median, and the error bars indicate the range. **i** Hemolysis of AMP 1003 on mouse red blood cells, $n = 3$ independent replicates. Data are presented as mean values ± SD. Data points show the individual values, the central line represents the median, and the error bars indicate the range. **j**–**l** Cytotoxicity of AMP 1003 for BV-2, RAW 264.7 and HK-2 cells, $n = 3$ independent replicates. Data are presented as mean values ± SD. Data points show the individual values, the central line represents the median, and the error bars indicate the range. **m** Live/dead fluorescence images of BV-2 cells after treatment with various concentrations of AMP 1003. SYTO-9 stains only live cells and emits green fluorescence, whereas PI binds to dead cells and emits red fluorescence. $n = 3$ independent replicates. Scale bar: 200 μm. Source data are provided as a Source Data file.

secondary structures are not an absolute requirement for antimicrobial function. Many natural AMPs exhibit structural flexibility or disorder while maintaining potent activity[29,34].

AMP 1003 exhibiting promising antimicrobial activity, selectivity and stability

The antimicrobial activity of AMP 1003 was assessed by determining the minimum inhibitory concentration (MIC) against standard and clinically isolated multidrug-resistant bacteria. The peptide exhibited significant broad-spectrum antimicrobial activity, particularly against *MRSA* ATCC 33591 and *K. pneumoniae* ATCC 700603, with low MIC values of 8 μM (7.60 mg/L) (Fig. 1c, d and Supplementary Figs. 4 and 5). Further evaluation of its antimicrobial activity against various clinical isolates of multidrug-resistant *MRSA* and *K. pneumoniae* revealed its potent antimicrobial activity. As evidenced in Fig. 1c, d and Supplementary Fig. 4, AMP 1003 demonstrated commendable antimicrobial activity against *MRSA* MDR1-6 and *K. pneumoniae* MDR1-5, with MIC values in the range of 4–8 μM (7.60–15.19 mg/L) and 16–128 μM (30.38–243.07 mg/L), respectively, which was significantly superior to antibiotics that exhibited higher MIC values (such as tobramycin, gentamicin, ciprofloxacin, levofloxacin, imipenem, etc.) or lacked antimicrobial activity (such as piperacillin, cefotaxime). Additionally, the peptide exerted rapid bactericidal activity against both *MRSA* ATCC 33591 and *K. pneumoniae* ATCC 700603, as well as superior efficacy against clinical isolates of multidrug-resistant *MRSA* MDR2 and *K. pneumoniae* MDR5 compared to vancomycin (against *MRSA* MDR2) and polymyxin B (against *K. pneumoniae* MDR5) (Fig. 1e–h and Supplementary Fig. 6).

The biocompatibility of AMP 1003 was evaluated by hemolytic toxicity and cytotoxicity assays. As indicated in Fig. 1i, it displayed negligible hemolytic toxicity with HC_{10} values (the minimum concentration causing 10% hemolysis) exceeding 2048 μM, as well as exhibited low cytotoxicity characterized by IC_{50} values of 64 μM (for BV-2 cells) and 128 μM (for RAW 264.7 cells or HK-2 cells) (Fig. 1j–l). To conduct a more comprehensive examination of the toxicity of AMP 1003, we utilized BV-2 cells to perform live/dead staining tests. We demonstrated no obvious cell death induced by the peptide despite showing a slight decrease in cell density (Fig. 1m). To further quantify its selectivity, the selectivity index (SI) was calculated as the ratio of HC_{10} or IC_{50} to GM (the geometric mean of MIC). Notably, it demonstrated a better selectivity index ($HC_{10}/GM > 512$, $IC_{50}/GM = 8$ for BV-2 cells, $IC_{50}/GM = 16$ for RAW264.7 cells or HK-2 cells) (Supplementary Fig. 7). These findings suggested that AMP 1003 emerged as a promising antimicrobial candidate, consistent with previous reports that an ideal antimicrobial agent is considered highly valuable for clinical application and research when its SI exceeds 10[35].

Improving stability was the initial intention of this study. Stability testing revealed that AMP 1003 effectively evaded protease degradation with more than 90% of remained peptide after 6 h of exposure to trypsin, chymotrypsin, or pepsin, achieving higher stability than (WRK)4 that retained less than 10% of remained peptide after similar processing, due to the transformation of amino acid configurations from L-type to D-type (Fig. 2a, b). The tolerance concentration to trypsin of AMP 1003 was increased by at least 10^6 times compared to (WRK)4 (Supplementary Fig. 9a). Additionally, its antimicrobial activity remained unaffected when exposed to trypsin, chymotrypsin, or pepsin ranging from 1–8 mg/mL, with MICs fluctuating only within a 2-fold range at the highest tested protease concentration (Fig. 2c–e). Comparatively, the antimicrobial activity of (WRK)4 was significantly compromised even at the lowest concentration of trypsin, chymotrypsin, or pepsin (Supplementary Fig. 9b). Complex salt ions in physiological environments harm the antimicrobial activity of peptides, thereby limiting their therapeutic potential[21,25]. We tested the MICs of AMP 1003 against *MRSA* ATCC 33591 and *K. pneumoniae* ATCC 700603 under physiological salt conditions. As illustrated in Fig. 2f, g, no observable variations were found in its antimicrobial activity in the presence of Na^+ at a concentration of 0.25–4 mg/mL or Mg^{2+} at a concentration of 25–800 μg/mL, except that its MICs rose to 2-fold in 8 mg/mL of Na^+. The findings aligned with prior research that monovalent salt ions inhibit peptide binding to bacterial membranes at physiological concentrations[24]. Additionally, serum is known to attenuate the antimicrobial activity of AMPs through competition with bacterial membranes for electrostatic interactions[36]. Accordingly, the antimicrobial activity of AMP 1003 in mouse serum (Fig. 2h), Fetal Bovine Serum (FBS) (Fig. 2i), and Special Newborn Calf Serum (NBCS) (Fig. 2j) against *MRSA* ATCC 33591 and *K. pneumoniae* ATCC 700603 was assessed. The antimicrobial activity of the peptide remained unchanged upon incubation with 5% or 10% serum and the MIC values only exhibited a fluctuation within a range of 2- to 4-fold in the presence of 20% serum. This can be attributed to the fact that AMP 1003 possessed more positive charges, although negatively charged serum albumin competed with the electrostatic interactions between it and anionic bacterial membranes[37]. These findings highlighted the significant enhancement of stability and resistance to enzymatic degradation achieved by transforming amino acid configurations from L-type to D-type.

AMP 1003 alleviating antimicrobial resistance

Combination therapy utilizing antibiotics has emerged as a prevalent strategy to combat drug-resistant bacteria in clinical practice. Nonetheless, this strategy risks inducing resistance to both antibiotics in the combination. Previous studies have identified specific molecules, known as "resistance disruptors" that can restore antibiotic efficacy by inhibiting bacterial resistance or enhancing antimicrobial activity[38]. Unlike traditional antibiotics that target specific bacterial components, AMPs operate efficacy against drug-resistant bacteria and are less prone to resistance owing to a non-receptor-mediated membrane mechanism[39]. Additionally, AMPs have been shown to enhance antibiotic sensitivity in resistant bacteria and alleviate antimicrobial resistance through their unique mechanisms, including bacterial membrane disruption and efflux pump system inactivation[40].

In the current study, AMP 1003 demonstrated superior antimicrobial activity against clinical isolates of multidrug-resistant strains compared to some conventional antibiotics, which displayed varying resistance levels (Fig. 1c, d). This observation prompted an investigation into whether the peptide modulated the antimicrobial resistance of these conventional antibiotics. Initially, a checkerboard assay was conducted to assess the synergistic effects of AMP 1003 in

https://doi.org/10.1038/s41467-025-65449-w

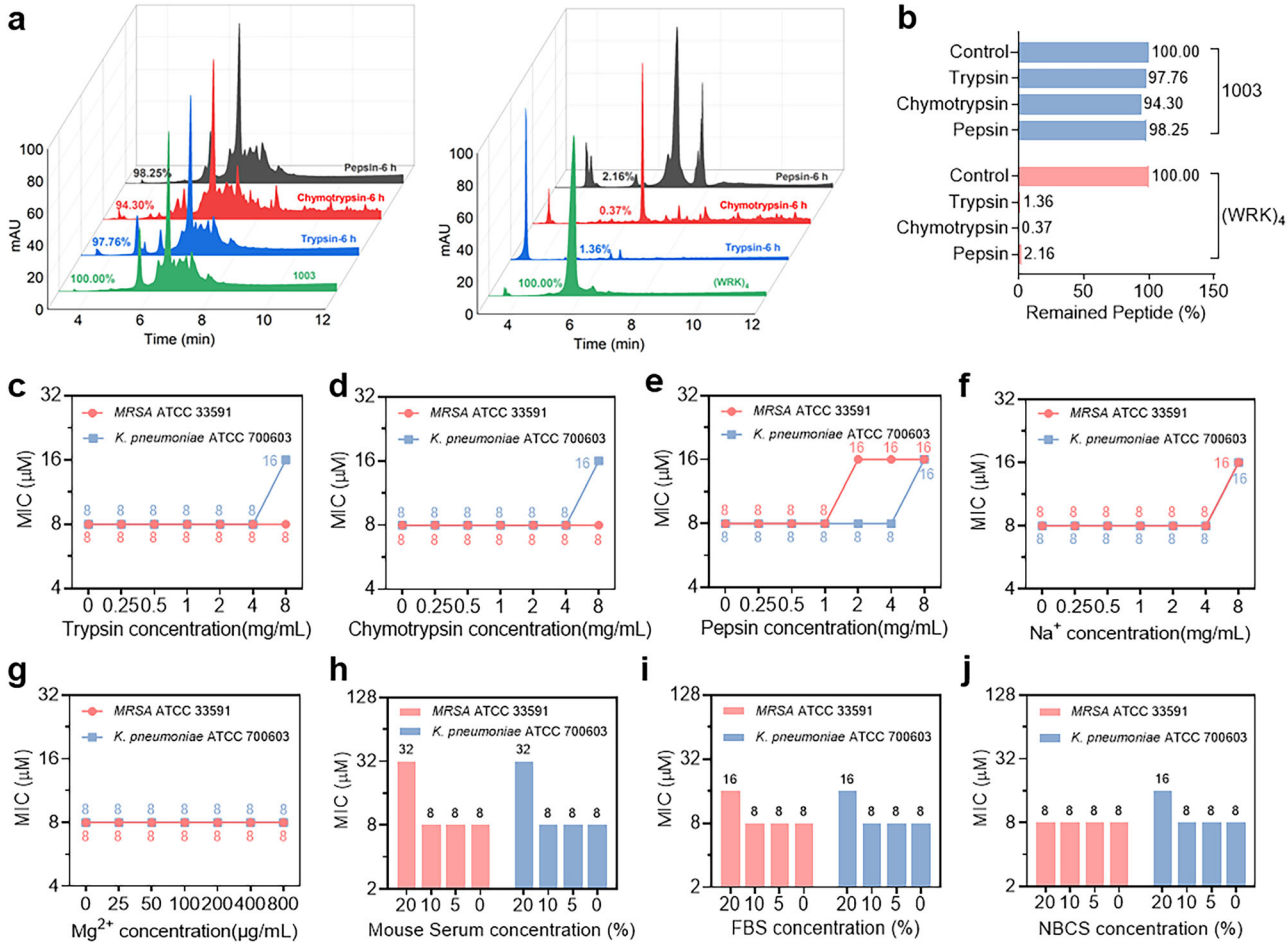

Fig. 2 | AMP 1003 displays high stability. a, **b** RP-HPLC analysis of AMP 1003 and (WRK)4 after incubation with trypsin, chymotrypsin and pepsin for 6 h at 37 °C. MICs of AMP 1003 against *MRSA* ATCC 33591 and *K. pneumoniae* ATCC 700603 in the presence of trypsin (**c**), chymotrypsin (**d**), pepsin (**e**), Na^+ (**f**), Mg^{2+} (**g**), mouse serum (**h**), FBS (**i**) and NBCS (**j**). Source data are provided as a Source Data file.

combination with antibiotics. As depicted in Fig. 3a, b, it exerted synergistic or additive antimicrobial activity in combination with these conventional antibiotics against both standard strains (*MRSA* ATCC 33591 and *K. pneumoniae* ATCC 700603) and multidrug-resistant clinical isolates (*MRSA* MDR2 and *K. pneumoniae* MDR5), except in combination with piperacillin against *K. pneumoniae* ATCC 700603 and *K. pneumoniae* MDR5, with tobramycin against *K. pneumoniae* ATCC 700603, or polymyxin B against *K. pneumoniae* ATCC 700603 (FICIs were more than 1). These results indicated that AMP 1003 can alleviate resistance (FICI < 0.5) or enhance susceptibility (0.5 ≤ FICI ≤ 1.0) of conventional antibiotics.

Subsequent to this, the impact of AMP 1003 on the development of bacterial resistance was evaluated via an induced resistance assay over 14 passages. Continuous exposure to the peptide at 1/2 × MIC did not induce obvious resistance in *MRSA* ATCC 33591 or *K. pneumoniae* ATCC 700603, with MICs showing no more than a 4-fold increase (Fig. 3c, d and Supplementary Fig. 10). In contrast, significant resistance was developed against *MRSA* ATCC 33591 after continuous 14 passages exposure to cefotaxime (up to 8-fold increases in MIC), gentamicin (up to 128-fold increases in MIC), and imipenem (up to 8-fold increases in MIC), and *K. pneumoniae* ATCC 700603 after continuous 14 passages exposure to ciprofloxacin (up to 64-fold increases in MIC), cefotaxime (up to 256-fold increases in MIC), gentamicin (up to 512-fold increases in MIC), imipenem (up to 16-fold increases in MIC), and minocycline (up to 8-fold increases in MIC). Combining AMP 1003 with antibiotics at 1/2 × MIC inhibited resistance development (Fig. 3c, d). Furthermore, we investigated the cross-resistance between the peptide and antibiotics. The results revealed no significant cross-resistance of AMP 1003 to final-generation strains exposed to ciprofloxacin, cefotaxime, gentamicin, imipenem, or minocycline, with MIC values remaining in the range of 4–16 μM (Supplementary Fig. 11a, b). However, notable cross-resistance was observed for gentamicin against the final generation of *MRSA* ATCC 33591 treated with the peptide, showing a 128-fold increase in MIC (Supplementary Fig. 11c). Similarly, gentamicin and imipenem exhibited significant cross-resistance to the final generation of *K. pneumoniae* ATCC 700603 treated with the peptide, with 16-fold and 8-fold increases in MIC, respectively (Supplementary Fig. 11d). Despite these instances of cross-resistance, AMP 1003 demonstrated synergistic or additive antimicrobial activity in combination with ciprofloxacin, cefotaxime, imipenem, and minocycline against the final-generation strains, with FICIs ranging from 0.1875 to 0.5625 (Supplementary Fig. 11e). In further chemo-sensitization studies, AMP 1003 at sub-inhibitory concentrations (1/4 × MIC, 1/2 × MIC) alleviated antibiotic resistance and restored sensitivity to antibiotics in multidrug-resistant bacteria, as evidenced by reductions in MICs (Supplementary Figs. 12–15). At the same time, it at sub-inhibitory concentrations (1/4 × MIC, 1/2 × MIC) significantly reduced the MICs of ciprofloxacin, cefotaxime, imipenem, and minocycline, effectively restoring the sensitivity of the final-generation *MRSA* ATCC 33591 and *K. pneumoniae* ATCC 700603 strains to these antibiotics (Supplementary Fig. 16).

https://doi.org/10.1038/s41467-025-65449-w

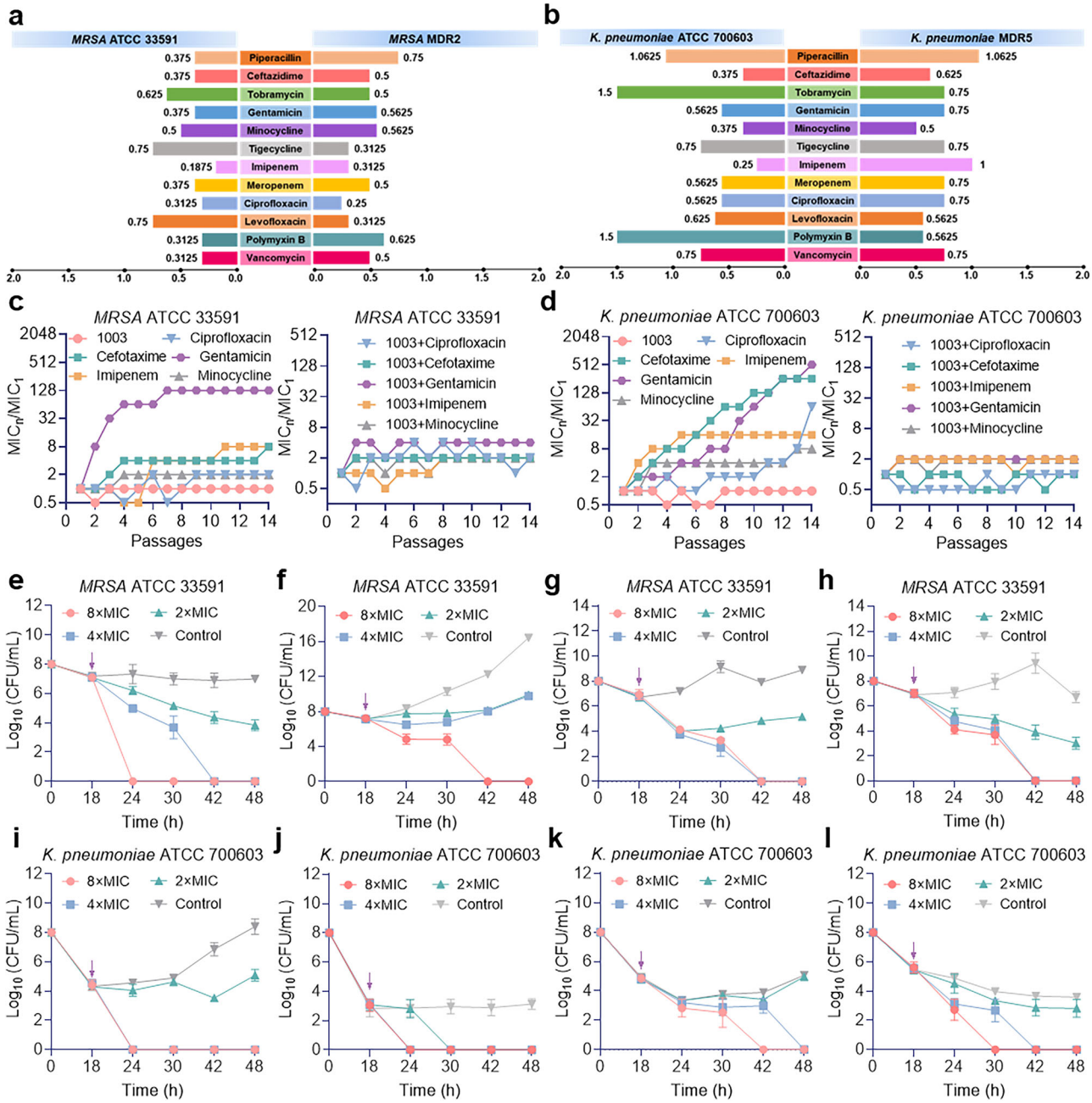

Fig. 3 | AMP 1003 alleviates antimicrobial resistance. a FICIs of AMP 1003 in combination with antibiotics against *MRSA* ATCC 33591 and *MRSA* MDR2. **b** FICIs of AMP 1003 in combination with antibiotics against *K. pneumoniae* ATCC 700603 *and K. pneumoniae* MDR5. Resistance development of *MRSA* ATCC 33591 (**c**) and *K. pneumoniae* ATCC 700603 (**d**) in the presence of sub-MIC concentration of AMP 1003, antibiotics, or their mixture. Killing kinetics of AMP 1003 against *MRSA* ATCC 33591 persister cells generated by 10 × MIC concentration of ciprofloxacin (**e**), gentamicin (**f**), imipenem (**g**) or minocycline (**h**) treatment, $n = 3$ independent replicates. Data are presented as mean values ± SD. Data points show the median, and the error bars indicate the range. Killing kinetics of AMP 1003 against *K. pneumoniae* ATCC 700603 persister cells generated by 10 × MIC concentration of ciprofloxacin (**i**), gentamicin (**j**), imipenem (**k**) or minocycline (**l**) treatment, $n = 3$ independent replicates. Data are presented as mean values ± SD. Data points show the median, and the error bars indicate the range. Source data are provided as a Source Data file.

Persister cells represent a subset of bacteria capable of withstanding high doses of antibiotics, complicating the treatment of bacterial infections[41]. The efficacy of AMP 1003 in eradicating bacterial persister cells was evaluated (Fig. 3e–l and Supplementary Fig. 17), demonstrating its ability to effectively eliminate or inhibit persister cells of *MRSA* ATCC 33591 and *K. pneumoniae* ATCC 700603 that survived exposure to high doses of various antibiotics in a concentration- and time-dependent manner. These antibiotics included ciprofloxacin, cefotaxime, gentamicin, imipenem, minocycline, and vancomycin for *MRSA* ATCC 33591, as well as ciprofloxacin, gentamicin, imipenem, minocycline, and polymyxin B for *K. pneumoniae* ATCC 700603. Bacteria frequently adhere to each other and form biofilms during the later stages of growth through the secretion of extracellular matrix, compromising the efficacy of antibiotics and contributing to antimicrobial resistance[4]. In the study, as illustrated in Supplementary Fig. 18, AMP 1003 exhibited significant biofilm inhibition activity against *MRSA* ATCC 33591 at 4 × MIC, demonstrating anti-biofilm activity comparable to vancomycin and ciprofloxacin.

AMP 1003 performing multiple antimicrobial mechanisms

In light of the findings above, the superior antimicrobial efficacy of AMP 1003 prompted a more in-depth investigation of its underlying mechanism. Disrupting the integrity of bacterial membranes is a well-established mechanism of cationic AMPs to exert antimicrobial activity[42], which is hypothesized to be the mode of action for AMP 1003. To explore this, we initially examined the interaction between the peptide and lipopolysaccharides (LPS, an abundant component of outer membranes in gram-negative bacteria) or lipoteichoic acids (LTA, an abundant component of cell wall in gram-positive bacteria) (Fig. 4a). The antimicrobial activity of AMP 1003 demonstrated a dose-dependent inhibition as the concentration of LPS or LTA increased to 128 μg/mL, with no discernible distinction between them. This observation aligned with its broad-spectrum antimicrobial efficacy. Comparatively, even at the highest detection concentration 1024 μg/mL, the peptide exhibited an inability to interact with phosphatidylcholine (PC, an abundant component of mammalian cell membranes), further highlighting its superior antimicrobial selectivity.

The outer membrane permeability of AMP 1003 was continuously evaluated using the hydrophobic fluorescent probe N-Phenyl-1-naphthylamine (NPN), which typically exhibited weak fluorescence in a hydrophilic extracellular environment but displayed significant fluorescence upon interaction with the hydrophobic environment within bacterial intracellular compartments[43]. As manifested in Fig. 4b, treatment with AMP 1003 resulted in a dose-dependent increase in the outer membrane permeability of *K. pneumoniae* ATCC 700603, as evidenced by rapid NPN uptake. Additionally, membrane depolarization was analyzed using 3,3′-dipropylthiadicarbocyanine iodide ($DiSC_3$-5), a membrane potential indicator[44]. The results indicated that AMP 1003 induced concentration-dependent alterations in the membrane potential of *MRSA* ATCC 33591 and *K. pneumoniae* ATCC 700603 (Fig. 4c, d). These effects were notably distinct from those observed with vancomycin and polymyxin B (Supplementary Fig. 19).

The effect of AMP 1003 on the integrity of the bacterial membrane was investigated utilizing SYTO-9/PI dye, which served as a live/dead bacterial indicator. The analysis of the red fluorescence signal emitted by PI demonstrated a concentration-dependent uptake of PI in *MRSA* ATCC 33591 and *K. pneumoniae* ATCC 700603 following treatment with AMP 1003, indicating damage to membrane integrity and subsequent bacterial death (Fig. 4e, f). In contrast, untreated bacteria (control group) only incorporated SYTO-9, emitting a green fluorescence signal (Fig. 4e, f). To investigate further, representative monoclonal populations of *MRSA* ATCC 33591 and *K. pneumoniae* ATCC 700603 were analyzed for SYTO-9 and PI signal intensity. *MRSA* ATCC 33591's PI signal was more potent at 4 × MIC of AMP 1003 compared to 2 × MIC, with no SYTO-9 signal at either concentration (Fig. 4g). Similarly, in *K. pneumoniae* ATCC 700603, the PI signal at 4 × MIC of the peptide was more intense than at 2 × MIC, with no SYTO-9 signal detected at 4 × MIC. However, at 2 × MIC, the intensities of PI and SYTO-9 signals were comparable (Fig. 4h). Control bacteria for both strains displayed a significant SYTO-9 signal (Fig. 4g, h). Additionally, the fluorescence intensity of PI was quantified using a microplate reader to evaluate the extent of membrane disruption caused by AMP 1003. Compared to the control group, treatment with the peptide resulted in a significant, concentration-dependent increase in fluorescence intensity of PI in both *MRSA* ATCC 33591 and *K. pneumoniae* ATCC 700603 (Fig. 4i, j). Afterwards, the morphological alterations of *MRSA* ATCC 33591 and *K. pneumoniae* ATCC 700603 upon exposure to AMP 1003 were examined using scanning electron microscopy (SEM). As shown in Fig. 4k, l, the untreated bacterial cells exhibited intact and smooth membranes. Conversely, bacteria treated with the peptide displayed significant surface irregularities, including wrinkles, pits, holes, and, in some cases, complete lysis. These observations further implied that AMP 1003 exerted antimicrobial effects by compromising bacterial membrane integrity.

A DNA-binding assay was initially conducted to investigate the effect of AMP 1003 on bacterial intracellular vitality. The results demonstrated that the peptide exhibited high binding affinity to the genomic DNA of *MRSA* ATCC 33591 and *K. pneumoniae* ATCC 700603, even at 2 × MIC (Fig. 5a), which suggested a possible bactericidal activity through interaction with bacterial DNA and interfering with the transcription process. DNA binding is known to trigger the release of reactive oxygen species (ROS) in bacteria[45], which can lead to direct membrane damage or induce bacterial apoptosis[46]. To further investigate this phenomenon, the generation of ROS was analyzed using 2′,7′-dichlorofluorescin diacetate (DCFH-DA)[47]. In *MRSA* ATCC 33591, treatment with AMP 1003 at 2 × MIC and 4 × MIC resulted in a significant increase in ROS accumulation (Fig. 5b). Notably, at 4 × MIC, the elevated ROS levels induced by the peptide were effectively suppressed by 5 mM N-Acetyl-L-cysteine (NAC, a typical antioxidant). In contrast, vancomycin had no such effect (Supplementary Fig. 20a). Similarly, in *K. pneumoniae* ATCC 700603, the level of ROS accumulation exhibited a significant increase upon treatment with the peptide at 1 × MIC, 2 × MIC and 4 × MIC, and was inhibited by 5 mM NAC (Fig. 5c). For polymyxin B, ROS elevation was observed only at 2 × MIC and 4 × MIC, and was also suppressed by NAC (Supplementary Fig. 20b). Taken together, the significant increase in ROS accumulation and the resulting bacterial damage underscore the intricate interplay of DNA binding, oxidative stress, and membrane disruption in the bactericidal action of AMP 1003.

The compromised integrity of bacterial membranes may potentially result in the leakage of intracellular contents. As illustrated in Fig. 5d–g, AMP 1003 caused a significant increase in UV absorbance at 260 nm and 280 nm in *MRSA* ATCC 33591 and *K. pneumoniae* ATCC 700603, in comparison to vancomycin and polymyxin B (Supplementary Fig. 21), indicating the leakages of intracellular nucleic acids and proteins of bacteria. Generally known, membrane damage considerably disrupts bacterial energy metabolism. To explore this, extracellular and intracellular ATP levels were quantified, as ATP serves as a critical energy signaling molecule. As shown in Fig. 5h–k, treatment with AMP 1003 at 2 × MIC, 4 × MIC and 8 × MIC resulted in a marked increase in extracellular ATP levels, accompanied by a corresponding reduction in intracellular ATP levels in both *MRSA* ATCC 33591 and *K. pneumoniae* ATCC 700603.

Collectively, the above findings suggested that the antimicrobial activity of AMP 1003 commenced with its electrostatic interaction with LPS or LTA on the bacterial membrane surface. This initial attraction facilitated the insertion of the peptide into the bacterial membrane, disrupting the outer, inner, and cytoplasmic membranes due to its hydrophobic properties, ultimately compromising membrane integrity. Following membrane disruption, it entered bacteria and interfered with intracellular biological processes, including hindering DNA replication, inducing ROS accumulation to promote oxidative damage, causing leakage of cellular contents, and disrupting ATP balance. Together, these mechanisms culminated in bacterial death, effectively exerting the antimicrobial activity of AMP 1003 (Fig. 5l).

Transcriptome analysis of *MRSA* or *K. pneumoniae* treated with AMP 1003

We further investigated the transcriptional changes in *MRSA* ATCC 33591 or *K. pneumoniae* ATCC 700603 treated with AMP 1003 at 4 × MIC and 2 × MIC utilizing the RNA-seq transcriptome sequencing technique. In the case of *MRSA* ATCC 33591, the transcript profile presented in the volcano plot showed that *MRSA* ATCC 33591 treated with the peptide at 4 × MIC expressed 546 upregulated genes and 341 downregulated genes, while expressed 258 upregulated genes and 44 downregulated genes at 2 × MIC, consistent with the concentration-dependent pattern of its antimicrobial effects (Fig. 6a–c). Notably, it was observed that the upregulated genes were associated with membrane repair. For instance, the gene responsible for the synthesis of the

https://doi.org/10.1038/s41467-025-65449-w

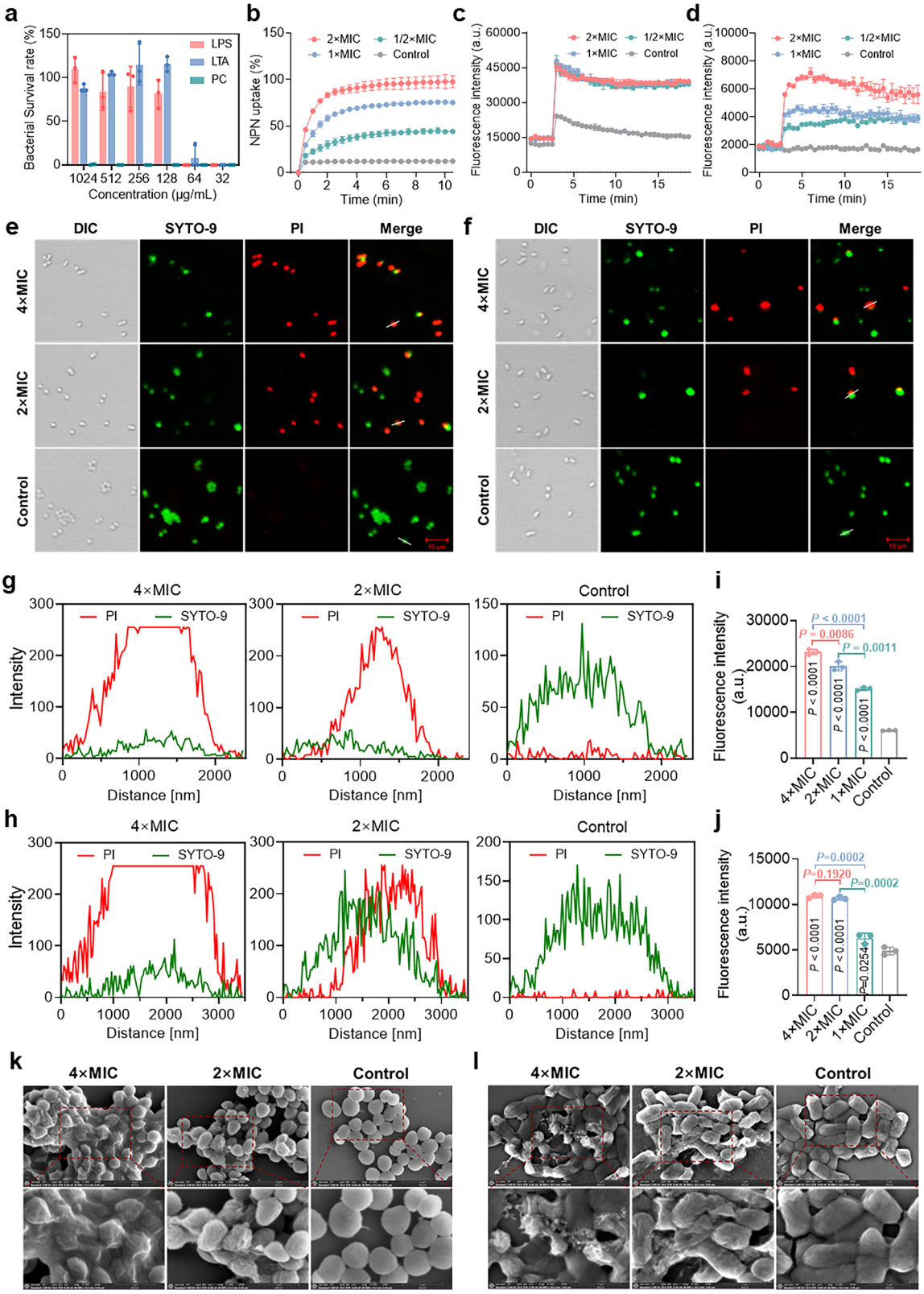

cell wall inhibition responsive protein *CwrA* was significantly upregulated $\log_2$[Fold change] = 5.78 at 4 × MIC and $\log_2$[Fold change] = 4.55 at 2 × MIC)[48], and the responsible of phospholipase was also upregulated $\log_2$[Fold change] = 4.30 at 4 × MIC and $\log_2$[Fold change] = 3.52 at 2 × MIC)[49]. Additionally, we noted an increased expression of genes encoding heat shock response proteins (*Hsp20* family protein), which detect and mitigate various insults, enhancing antibiotic uptake, protein aggregation, and ROS production[50]. Furthermore, the downregulation of genes associated with the metabolism of sugar ABC transporter permease, glyceraldehyde-3-phosphate dehydrogenase, and sn-glycerol-3-phosphate ABC transporter ATP-binding protein *UgpC* were observed under the treatment of AMP 1003. This finding aligned with previous research indicating that the decreased levels of glycerol-3-phosphate contribute to antibiotic tolerance[51].

Fig. 4 | Membrane targeting mechanisms of AMP 1003. a LPS/LTA/PC competitive inhibition of AMP 1003 against *MRSA* ATCC 33591, $n = 3$ independent replicates. Data are presented as mean values ± SD. Data points show the individual values, the central line represents the median, and the error bars indicate the range. **b** Outer membrane permeation effect of AMP 1003 on *K. pneumoniae* ATCC 700603, $n = 3$ independent replicates. Data are presented as mean values ± SD. Data points show the median, and the error bars indicate the range. Cytoplasmic membrane electrical potential of *K. pneumoniae* ATCC 700603 (**c**) and *MRSA* ATCC 33591 (**d**) treated with AMP 1003 at 2 × MIC, 1 × MIC, and 1/2 × MIC concentrations, $n = 3$ independent replicates. Data are presented as mean values ± SD. Data points show the median, and the error bars indicate the range. The confocal fluorescent images of *MRSA* ATCC 33591 (**e**) or *K. pneumoniae* ATCC 700603 (**f**) treated with AMP 1003 at 4 × MIC or 2 × MIC for 2 h with SYTO-9/PI dye. $n = 3$ independent replicates. Scale bar: 10 μm. **g** Overall fluorescence distribution curve in the marked region of **e** for *MRSA* ATCC 33591. **h** Overall fluorescence distribution curve in the marked region of **f** for *K. pneumoniae* ATCC 700603. The PI fluorescence intensity of *MRSA* ATCC 33591 (**i**) or *K. pneumoniae* ATCC 700603 (**j**) treated with AMP 1003 at 4 × MIC, 2 × MIC, and 1 × MIC concentrations for 2 h, $n = 3$ independent replicates. Data are presented as mean values ± SD. Data points show the individual values, the central line represents the median, and the error bars indicate the range. Statistical analysis: two-tailed *t*-test. SEM micrographs of *MRSA* ATCC 33591 (**k**) or *K. pneumoniae* ATCC 700603 (**l**) at 4 × MIC or 2 × MIC for 2 h. $n = 3$ independent replicates. Source data are provided as a Source Data file.

Furthermore, the effect of the peptide on bacterial DNA has also been emphasized, as the gene responsible for the synthesis of DNA damage-induced cell division inhibitor *SosA* was upregulated ($\log_2$[Fold change] = 4.52 at 4 × MIC and $\log_2$[Fold change] = 3.22 at 2 × MIC) (Fig. 6d and Supplementary Fig. 22). Gene Ontology (GO) enrichment analysis showed the significant regulation of the genes involved in membrane, ABC transporters, transmembrane transport, DNA-binding transcription and proton-transporting ATP in *MRSA* ATCC 33591 after treatment with AMP 1003 (Fig. 6e). Kyoto Encyclopedia of Genes and Genomes (KEGG) enrichment analysis demonstrated that the pathways associated with membrane transport and metabolism were impacted by the peptide (Fig. 6f).

Similarly, the transcript profile of the volcano plot revealed *K. pneumoniae* ATCC 700603 treated with AMP 1003 in a concentration-dependent manner, with 65 genes being upregulated and 60 genes being downregulated at 4 × MIC, and 71 genes being upregulated and 38 genes being downregulated at 2 × MIC (Fig. 7a–c). It was determined that the downregulated genes were related to membrane permeability, including betaine-aldehyde dehydrogenase *betB* ($\log_2$[Fold change] = −1.74 at 4 × MIC and $\log_2$[Fold change] = −1.24 at 2 × MIC), choline dehydrogenase *betA* ($\log_2$[Fold change] = −1.99 at 4 × MIC and $\log_2$[Fold change] = −1.45 at 2 × MIC) and transcriptional regulator *betI* ($\log_2$[Fold change] = −1.56 at 4 × MIC and $\log_2$[Fold change] = −1.20 at 2 × MIC)[52]. Concurrently, downregulation of genes associated with energy metabolism was also observed, including anaerobic glycerol-3-phosphate dehydrogenase subunit *GlpC*, glycine betaine/L-proline ABC transporter ATP-binding protein *ProV*, glycine betaine/L-proline ABC transporter permease *ProW*, and glycine betaine/L-proline ABC transporter substrate-binding protein *ProX*[51]. Additionally, the gene responsible for superoxide response transcriptional regulator *SoxS* was downregulated, supporting the antimicrobial pattern of the peptide by promoting the generation of ROS to cause oxidative damage[53] (Fig. 7d and Supplementary Fig. 23). GO enrichment analysis showed the significant regulation of the genes involved in membrane, ABC transporters and transmembrane transport in *K. pneumoniae* ATCC 700603 post-treatment with the peptide (Fig. 7e). KEGG enrichment analysis presented that the peptide significantly affected the membrane transport, amino acid metabolism and carbohydrate metabolism of *K. pneumoniae* ATCC 700603, and the phenomenon was more significant at low concentrations (Fig. 7f). These results were consistent with our previous observations that AMP 1003 disrupted or damaged bacterial membrane and intracellular processes.

AMP 1003 exerting promising therapeutic potential in *MRSA*- or *K. pneumoniae*-infected pneumonia models

Building upon the superior antimicrobial performance of AMP 1003, we further assessed its efficacy in vivo via a pneumonia mouse model induced by *MRSA* ATCC 33591 or *K. pneumoniae* ATCC 700603 (Fig. 8a). Vancomycin and polymyxin B were utilized as positive controls for *MRSA* ATCC 33591 and *K. pneumoniae* ATCC 700603, respectively. Notably, the peptide significantly diminished bacterial loads in the lungs of *MRSA* ATCC 33591-infected pneumonia mice at doses of 5 mg/kg and 10 mg/kg, with bacterial loads decreased by approximately 1.64-$\log_{10}$CFU and 2.79-$\log_{10}$CFU, respectively, comparable to vancomycin's reduction of 2.23-$\log_{10}$CFU at a dose of 5 mg/kg (Fig. 8b). Similarly, in *K. pneumoniae* ATCC 700603-infected pneumonia mice, the peptide reduced bacterial loads by 1.8-$\log_{10}$CFU at dose of 5 mg/kg and 2.73-$\log_{10}$CFU at a dose of 10 mg/kg, demonstrating comparable efficacy to polymyxin B with 1.58-$\log_{10}$CFU reduction at a dose of 5 mg/kg (Fig. 8d). Histological analysis further corroborated the therapeutic potential of AMP 1003. H&E staining revealed severe pulmonary lesions in model mice treated with saline, including bronchial epithelial damage, epithelial sloughing, severe bronchitis, and alveolar hemorrhage (Fig. 8c, e). In contrast, treatment with the peptide, vancomycin, or polymyxin B substantially alleviated these pathological changes, restoring lung tissue integrity to near-normal levels. This phenomenon is also reflected in the liver tissue adjacent to the lungs (Supplementary Fig. 24). These findings underscored the robust therapeutic potential of AMP 1003 in treating pneumonia caused by *MRSA* ATCC 33591 or *K. pneumoniae* ATCC 700603.

AMP 1003 presenting significant anti-inflammatory activity in vitro and in vivo

The inflammatory response triggered by bacterial infection represents a fundamental component of host immune defense, and its excessive activation can result in tissue damage and multi-organ dysfunction, particularly in light of the increasingly severe issues surrounding antibiotic resistance. Consequently, targeted regulatory strategies for host inflammatory pathways have garnered significant attention[54]. Thus, we evaluated the anti-inflammatory activity of AMP 1003 utilizing an LPS-induced inflammation model in RAW 264.7 cells (Fig. 9a). The data indicated that LPS significantly upregulated inflammatory levels of RAW 264.7 cells, followingly by treatment with the peptide resulting in a dose-dependent reduction, including *Il-1β* (Fig. 9b), *Tnf-α* (Fig. 9c), Il-*12* (Fig. 9d), Il-*17* (Fig. 9e), Il-*18* (Fig. 9f) and *iNOS* (Fig. 9g), underscoring the significant anti-inflammatory potential of AMP 1003.

Building upon these promising results in vitro, we assessed the in vivo anti-inflammatory efficacy of AMP 1003 in an LPS-induced acute lung injury mouse model (Fig. 9h). Following intratracheal spraying-challenging with LPS from *E. coli* O111:B4 (5 mg/kg), mice exhibited severe pulmonary lesions, including bronchial epithelial damage, epithelial sloughing, severe bronchitis, and alveolar hemorrhage (Fig. 9i). Notably, treatment with the peptide at a dose of 5 mg/kg significantly ameliorated these tissue lesions (Fig. 9i). Furthermore, levels of inflammatory cytokines in lung tissues were reduced following treatment. Specifically, the peptide significantly decreased the expression of *Tnf-α* (Fig. 9j), Il-1*β* (Fig. 9k), Il-*12* (Fig. 9l), *Mcp1* (Fig. 9m), and *Cd86* (Fig. 9n) compared to the LPS group.

AMP 1003 showing low toxicity in vivo

In addition to the above therapeutic efficacy studies, we also investigated its acute toxicity in vivo by a single intraperitoneal injection at doses of 20 mg/kg, 30 mg/kg or 40 mg/kg, with matched dosage

https://doi.org/10.1038/s41467-025-65449-w

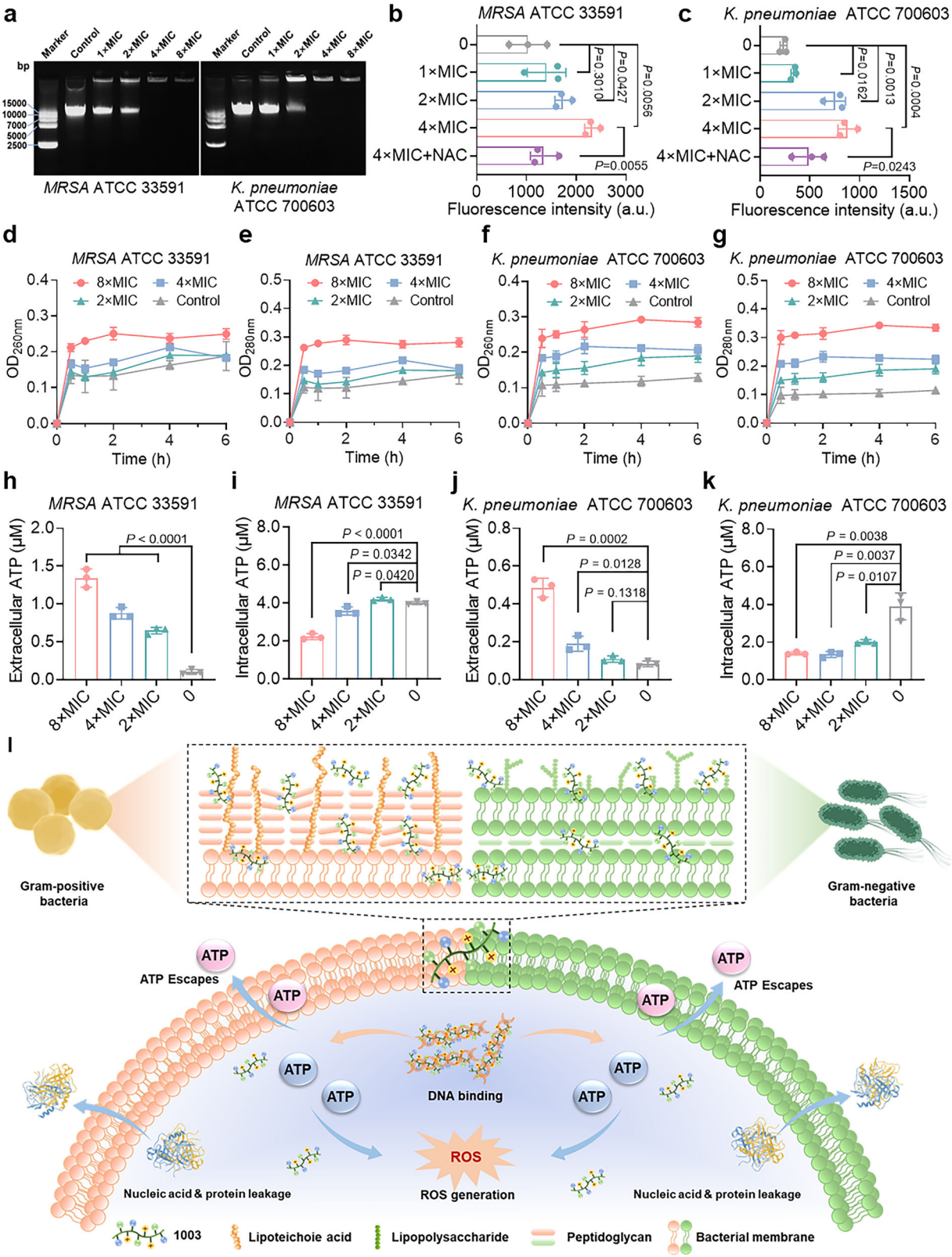

polymyxin B as control (Fig. 10a). At a dose of 20 mg/kg, 25% of the polymyxin B-treated mice exhibited ruffled fur and poor motility. Concurrently, the remaining subjects manifested severe symptoms, including hunching, fur ruffling and complete immobility in response to stimulation (Supplementary Fig. 25). Notably, administrations with AMP 1003 at the same dose did not result in any observable pathological changes over 7 days. At doses of 30 mg/kg or 40 mg/kg, all mice injected with polymyxin B displayed sluggish behavior and succumbed within 30–60 min (Supplementary Figs. 25 and 26a). In contrast, there was no mouse death after injection of AMP 1003 at a dose of 30 mg/kg. Only 25% of the mice administered the peptide at 40 mg/kg experienced mortality while the survivors exhibited temporary abnormal behaviors but remained alive for up to 7 days (Fig. 10a, b and Supplementary Fig. 25). Simultaneously, body weight monitoring over this

Fig. 5 | Non-membrane targeting mechanisms of AMP 1003. a DNA-binding ability of AMP 1003 to *MRSA* ATCC 33591 and *K. pneumoniae* ATCC 700603. $n = 3$ independent replicates. ROS accumulation of *MRSA* ATCC 33591 (**b**) and *K. pneumoniae* ATCC 700603 (**c**) treated with AMP 1003, $n = 3$ independent replicates. Data are presented as mean values ± SD. Data points show the individual values, the central line represents the median, and the error bars indicate the range. Statistical analysis: two-tailed *t*-test. Nucleic acid and proteins leak of *MRSA* ATCC 33591 (**d**, **e**) and *K. pneumoniae* ATCC 700603 (**f**, **g**) treated with AMP 1003, $n = 3$ independent replicates. Data are presented as mean values ± SD. Data points show the median, and the error bars indicate the range. Extracellular and intracellular ATP levels of *MRSA* ATCC 33591 (**h**, **i**) and *K. pneumoniae* ATCC 700603 (**j**, **k**) treated with AMP 1003, $n = 3$ independent replicates. Data are presented as mean values ± SD. Data points show the individual values, the central line represents the median, and the error bars indicate the range. Statistical analysis: two-tailed *t*-test. **l** Proposed antimicrobial mechanism of AMP 1003 against gram-positive and gram-negative bacteria. Source data are provided as a Source Data file.

period revealed no significant changes among the groups receiving 20 mg/kg or 30 mg/kg dose of both treatments. In the 40 mg/kg dose group, a transient weight loss was recorded at day 2, gradually returning to baseline levels thereafter (Fig. 10c and Supplementary Fig. 26b). Seven days after administration, serum analysis of surviving mice revealed no apparent hepatotoxicity in those treated with AMP 1003 at all injection doses and polymyxin B at 20 mg/kg, as evidenced by stable levels of alanine aminotransferase (ALT) and aspartate aminotransferase (AST) (Fig. 10d, e and Supplementary Fig. 25c, d). Additionally, the late biomarkers levels of nephrotoxicity (blood urea nitrogen (BUN) and serum creatinine (CREA)) in surviving mice following treatment with AMP 1003 (20 mg/kg, 30 mg/kg or 40 mg/kg) or polymyxin B (20 mg/kg) remained comparable to that of control group (Fig. 10f, g and Supplementary Fig. 25e, f). Further nephrotoxicity analysis revealed that both AMP 1003 and polymyxin B did not cause noticeable changes in early biomarkers neutrophil gelatinase-associated lipocalin (NGAL), Cystatin C and kidney injury molecule-1 (Kim-1) levels in mouse serum or urine at doses of 20 mg/kg or 30 mg/kg (Supplementary Fig. 28). There were no significant changes in the levels of *Cystatin C*, *Lipocalin 2* (the coding gene of NGAL), and *Havcr1* (the coding gene of Kim-1) mRNA in the kidneys of mice treated with AMP 1003 at doses of 20 mg/kg or 30 mg/kg. However, polymyxin B caused a notable increase in *Cystatin C* and *Lipocalin 2* mRNA levels at a 20 mg/kg dose, indicating nephrotoxicity (Supplementary Fig. 29). Histological analysis by H&E indicated that AMP 1003 primarily induced slight inflammatory cell infiltration in the lungs, hepatocyte necrosis with cellular swelling, and renal cell necrosis accompanied by tissue hemorrhage only at a dose of 40 mg/kg (Fig. 10h and Supplementary Fig. 27). Polymyxin B, in comparison, caused more severe tissue damage, including alveolar cavity wrinkling, pronounced inflammatory infiltration, lung and renal cell necrosis, hepatocyte necrosis, and cellular atrophy (Supplementary Fig. 26g). Meanwhile, renal tubular injury scores in mice administered with AMP 1003 at 20 mg/kg or 30 mg/kg were comparable to those of normal mice, with no significant difference. However, mice treated with polymyxin B at 20 mg/kg had significantly higher injury scores than normal mice (Supplementary Fig. 30), indicating increased tubular injury. The organ (heart, liver, spleen, lung, kidney) indices of mice treated with AMP 1003 or polymyxin B showed no statistically significant differences from the control group, while the organ index of liver in polymyxin B-treated mice was higher than that in the control group (Fig. 10i and Supplementary Fig. 26h). Additionally, investigations into drug distribution in metabolically active organs revealed a notable accumulation of AMP 1003 in the liver and kidneys, which gradually decreased over time (Fig. 10j, k).

Discussion

The escalating threat presented by multidrug-resistant bacterial infections, particularly regarding respiratory pathogens such as *MRSA* and *K. pneumoniae*, underscores the urgent necessity for innovative antimicrobial strategies. AMPs represent a promising candidate in combating multidrug-resistant bacterial infections owing to their broad antimicrobial efficacy and low tendency of bacterial resistance. However, their clinical application has persistently encountered substantial challenges, including susceptibility to proteases, cytotoxicity, and difficulty achieving an promising balance between efficacy and toxicity[28].

Building upon our previous development of peptide (WRK)4 featuring repeating tryptophan-arginine-lysine motifs through de novo design strategy and demonstrated potent antimicrobial activity and low toxicity but limited proteolytic stability[32], we implemented a targeted D-amino acid substitution strategy to engineer AMP 1003 with four repeating units of (D-tryptophan)-(D-arginine)-(D-lysine) in this study, thereby achieving a synergistic balance of enhanced stability, broad-spectrum antimicrobial efficacy, and biosafety. Unlike conventional D-amino acid modifications that frequently compromise antimicrobial activity or safety, our scaffold-centric approach has preserved the essential amphiphilic architecture. Specifically, the indole moieties of D-tryptophan maintain critical interfacial membrane interactions, while D-arginine and D-lysine sustain cationic charge density to facilitate electrostatic targeting of bacterial membranes[29,31]. This structural optimization has yielded AMP 1003, which exhibited notable resistance to proteolytic degradation without sacrificing antimicrobial potency. Furthermore, the peptide demonstrated broad-spectrum activity against clinically isolated multidrug-resistant bacteria, particularly *MRSA* (MIC: 4–8 μM (7.60–15.19 mg/L)) and *K. pneumoniae* (MIC: 16–128 μM (30.38–243.07 mg/L)), with results significantly superior to those observed with partial conventional antibiotics (Fig. 1c, d). Although its MIC values were slightly higher than those of vancomycin against *MRSA* and polymyxin B (against *K. pneumoniae*), it exhibited a faster bactericidal speed (Fig. 1e–h and Supplementary Fig. 5). It's important to note that AMP 1003 exhibited antimicrobial effects against both gram-positive (e.g., *S. aureus*) and gram-negative (e.g., *K. pneumoniae*) bacteria, including MDR strains. In contrast, the reference antibiotics are typically limited to specific bacterial strains (e.g., polymyxin B primarily targets gram-negative bacteria, vancomycin targets gram-positive bacteria). Additionally, the higher absolute MIC values (in mg/L) for AMP 1003 partially reflect its larger molecular size, but its molar activity (μM) remains relevant for mechanistic studies. Importantly, AMP 1003 maintained exceptional biocompatibility, exhibiting negligible hemolytic toxicity (<5% hemolysis at 2048 μM) and low cytotoxicity (IC_{50}: 64–128 μM), which was superior to that of melittin (which caused cytotoxicity and hemolysis at merely 2 μM) even though it exhibited better antimicrobial potency (MIC: 1–16 μM) against multidrug-resistant bacteria with lower stability[32,44]. This underscored the necessity of breaking free from the constraints typically associated with traditional AMPs' "high efficiency and high toxicity"[28].

The rapid evolution of bacterial resistance has emerged as a significant challenge to global public health, with many bacteria exhibiting increasing resistance to traditional antibiotics (such as beta-lactams and fluoroquinolones) as well as last-line defense drugs (such as vancomycin and polymyxin B)[12,55]. Although AMPs are less likely to induce bacterial resistance due to their action targeting bacterial membranes, even a single membrane targeting mechanism may still facilitate adaptive bacterial resistance through various pathways[56]. In this study, AMP 1003 displayed significant advantages in inhibiting the evolution of bacterial resistance. Continuous passage experiments indicated that its MICs against *MRSA* ATCC 33591 and *K. pneumoniae* ATCC 700603 did not increase after 15 passages, contrasting sharply

https://doi.org/10.1038/s41467-025-65449-w

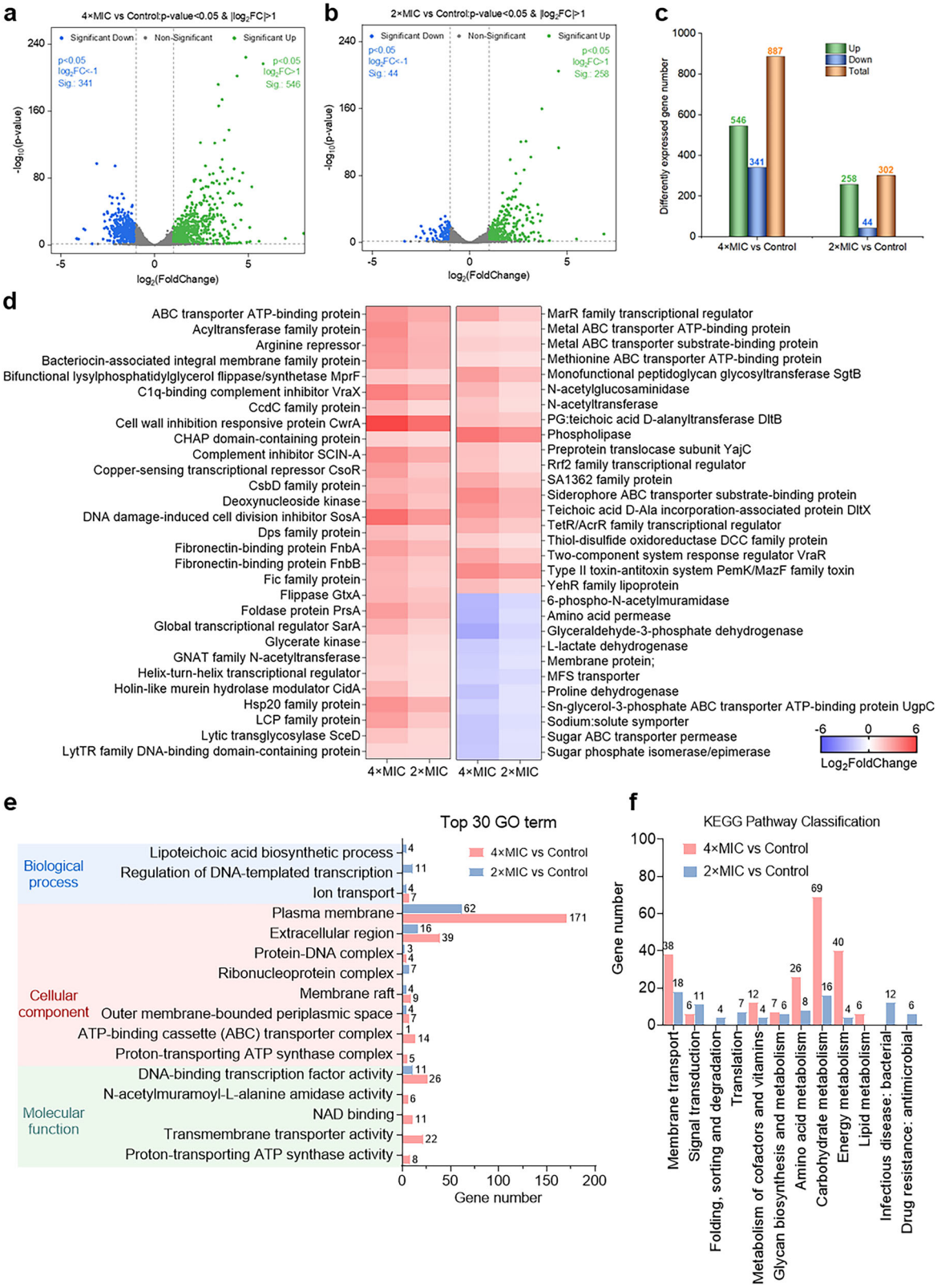

Fig. 6 | Transcriptome analysis of *MRSA* ATCC 33591 under the treatment of AMP 1003. a, **b** Volcanic map of transcriptional differential genes. Genes are identified as significantly different between the treatment of AMP 1003 at 4 × MIC and 2 × MIC, with $p < 0.05$ and $|\log_2[\text{Fold change}]| > 1$ in expression level. Statistical analysis: two-tailed *t*-test. **c** Differently expressed genes under different concentrations of AMP 1003 treatment vs. control. **d** Heat map analysis of representative, differently expressed genes. **e** GO enrichment analysis of differentially expressed genes (Top 30). **f** KEGG enrichment analysis of differentially expressed genes. $n = 3$ biological replicates. Data are presented as means. Source data are provided as an NCBI database with SRA accession code: PRJNA1224220.

https://doi.org/10.1038/s41467-025-65449-w

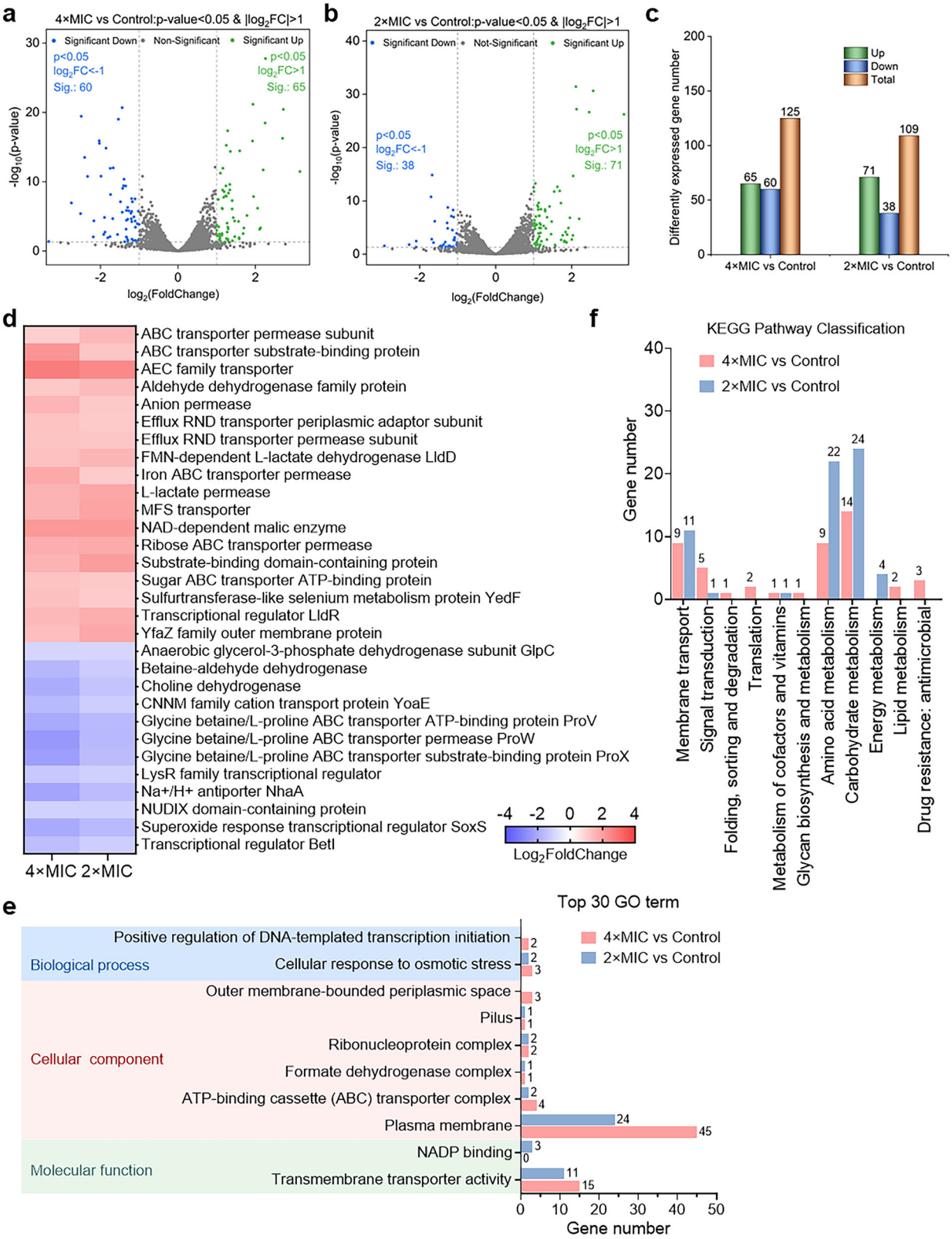

Fig. 7 | Transcriptome analysis of *K. pneumoniae* ATCC 700603 under the treatment of AMP 1003. a, **b** Volcanic map of transcriptional differential genes. Genes are identified as significantly different between the treatment of AMP 1003 at 4 × MIC and 2 × MIC concentrations, with $p < 0.05$ and $|\log_2[\text{Fold change}]| > 1$ in expression level. Statistical analysis: two-tailed *t*-test. **c** Differently expressed genes under different concentrations of AMP 1003 treatment vs. control. **d** Heat map analysis of representative, differently expressed genes. **e** GO enrichment analysis of differentially expressed genes (Top 30). **f** KEGG enrichment analysis of differentially expressed genes. $n = 3$ biological replicates. Data are presented as means. Source data are provided as an NCBI database with SRA accession code: PRJNA1224220.

https://doi.org/10.1038/s41467-025-65449-w

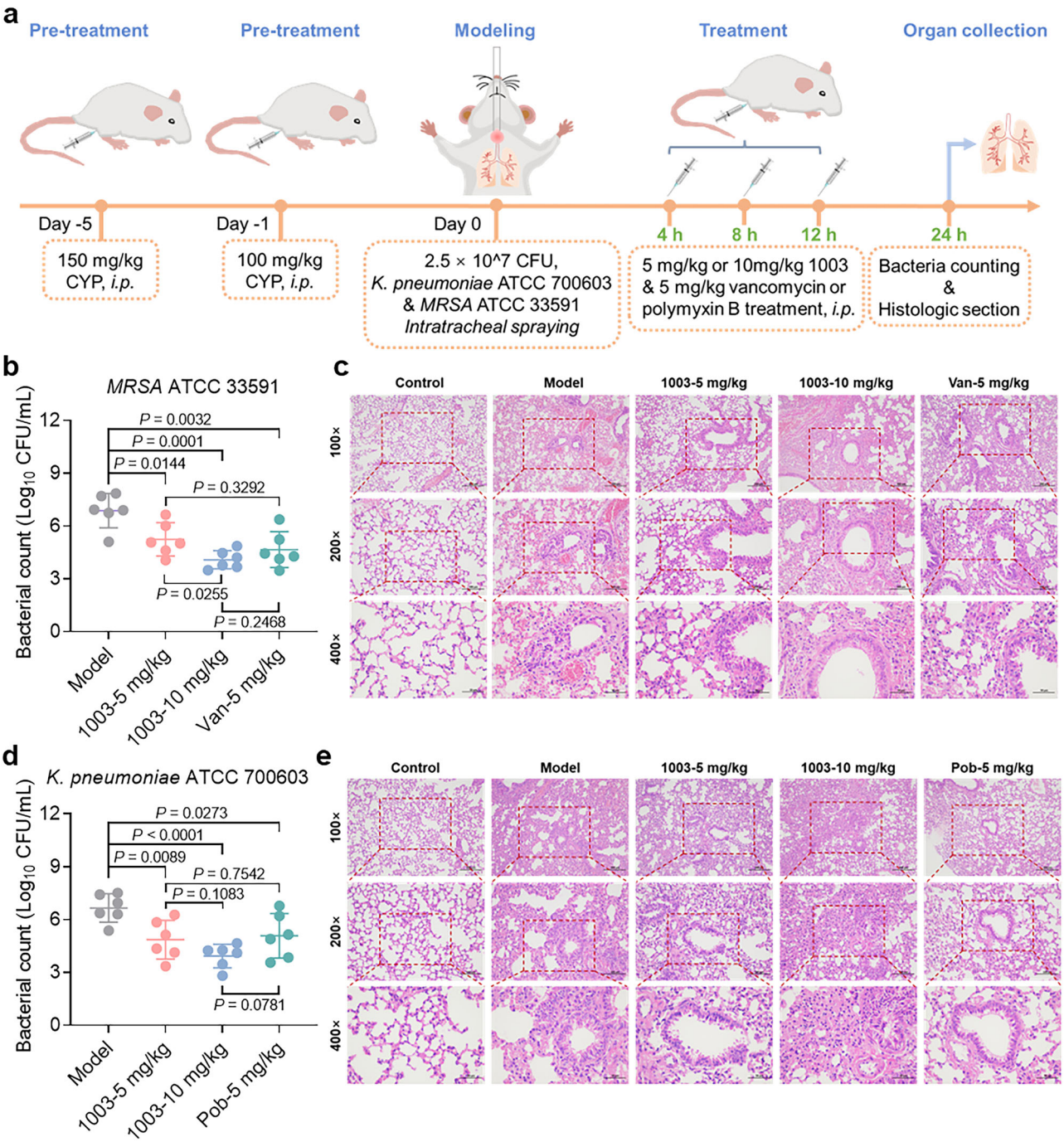

Fig. 8 | AMP 1003 exerts promising therapeutic potential in *MRSA*- or *K. pneumoniae*-infected pneumonia models. a Flowchart of the bacterial pneumonia experiment. CYP stands for cyclophosphamide. **b** Bacterial load (in terms of CFU/mL) in the lung homogenate of *MRSA* ATCC 33591-infected pneumonia mouse model treated with saline, 1003 (5 mg/kg or 10 mg/kg), or Van (5 mg/kg). Van stands for vancomycin, $n = 6$ mice per group. Data are presented as mean values ± SD. Data points show the individual values, the central line represents the median, and the error bars indicate the range. Statistical analysis: two-tailed *t*-test. **c** Pathological sections stained by H&E of the lung in the *MRSA* ATCC 33591-infected pneumonia mouse model treated with saline, 1003 (5 mg/kg or 10 mg/kg), or Van (5 mg/kg), Van stands for vancomycin, $n = 3$ mice per group. Scale bar: 100×: 200 μm, 200×: 100 μm, 400×: 50 μm. **d** Bacterial load (in terms of CFU/mL) in the lung homogenate of *K. pneumoniae* ATCC 700603-infected pneumonia mouse model treated with saline, 1003 (5 mg/kg or 10 mg/kg), or Pob (5 mg/kg). Pob stands for polymyxin B, $n = 6$ mice per group. Data are presented as mean values ± SD. Data points show the individual values, the central line represents the median, and the error bars indicate the range. Statistical analysis: two-tailed *t*-test. **e** Pathological sections stained by H&E of the lung in the *K. pneumoniae* ATCC 700603-infected pneumonia mouse model treated with saline, 1003 (5 mg/kg or 10 mg/kg), or Pob (5 mg/kg), Pob stands for polymyxin B, $n = 3$ mice per group. Scale bar: 100×: 200 μm, 200×: 100 μm, 400×: 50 μm. Source data are provided as a Source Data file.

with the rapid development of antibiotic resistance (Fig. 3c, d). Importantly, the peptide successfully suppressed the emergence of resistance to antibiotics, restored the antimicrobial efficacy of these antibiotics against multidrug-resistant bacteria, and effectively eliminated bacterial persister cells that had evaded antibiotic treatment (Fig. 3e–l and Supplementary Figs. 12–16). Mechanism studies demonstrated that AMP 1003 presented unique multiple antimicrobial mechanisms: firstly, the interaction between its amphiphilic structure

https://doi.org/10.1038/s41467-025-65449-w

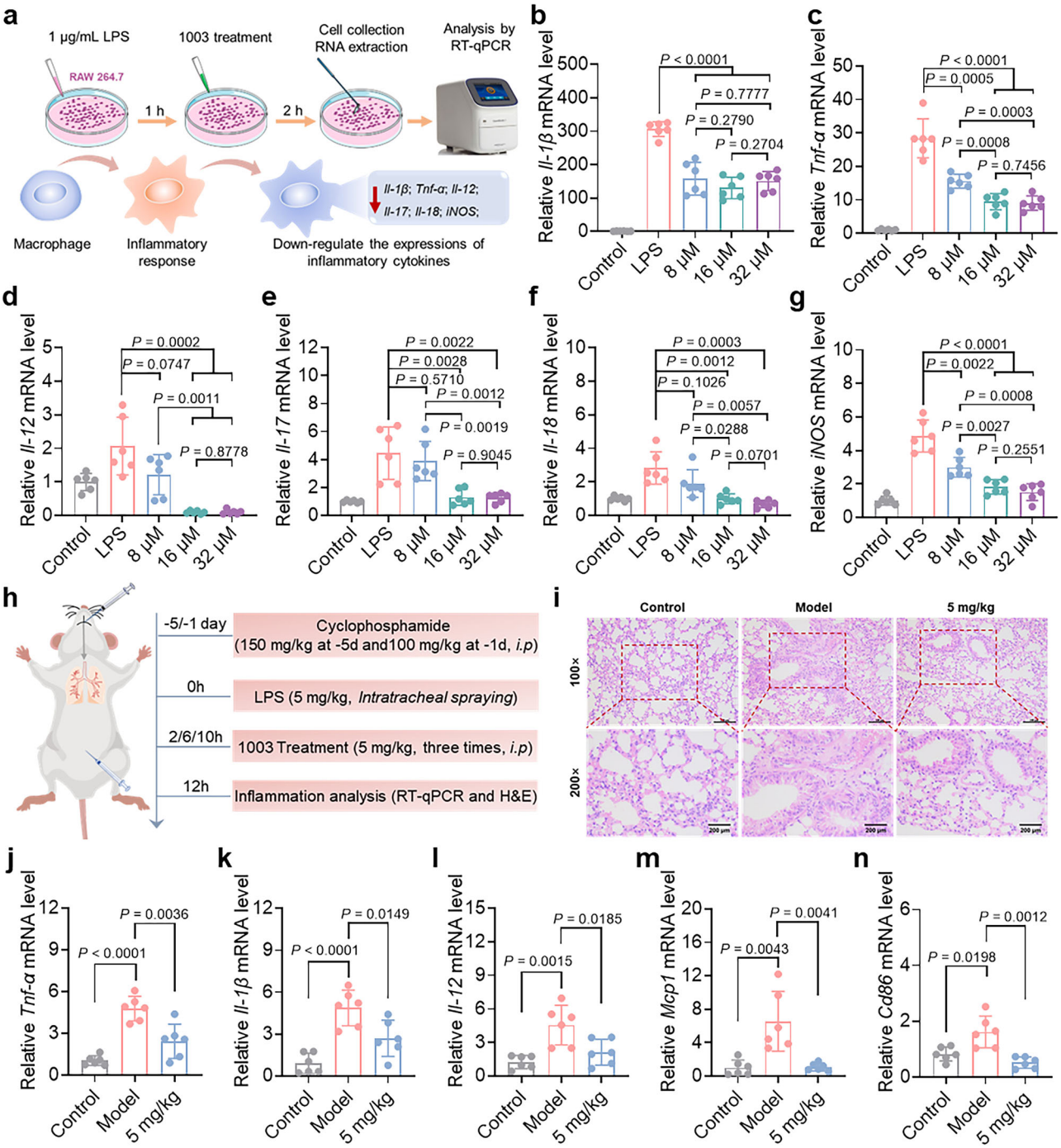

Fig. 9 | AMP 1003 presents significant anti-inflammatory activity in vitro and in vivo. a Flowchart of the anti-inflammatory activity in vitro of AMP 1003 in the LPS-induced inflammation model in RAW 264.7 cells. The relative *Il-1β* (**b**), *Tnf-α* (**c**), *Il-12* (**d**), *Il-17* (**e**), *Il-18* (**f**) and *iNOS* (**g**) levels of LPS-stimulated RAW264.7 cells after treatment with AMP 1003, $n = 6$ independent replicates. Data are presented as mean values ± SD. Data points show the individual values, the central line represents the median, and the error bars indicate the range. Statistical analysis: two-tailed *t*-test. **h** Flowchart of the anti-inflammatory activity in vivo of AMP 1003 in the LPS-induced acute lung injury mouse model. **i** Pathological sections stained by H&E of the lung in LPS-induced acute lung injury mice after treatment with AMP 1003 at a dose of 5 mg/kg, $n = 3$ mice per group. Scale bar: 100×: 100 μm, 200×: 200 μm. The relative *Tnf-α* (**j**), *Il-1β* (**k**), *Il-12* (**l**), *Mcp1* (**m**), and *Cd86* (**n**) levels of the LPS-induced acute lung injury mouse model after treatment with AMP 1003 at a dose of 5 mg/kg, $n = 6$ mice per group. Data are presented as mean values ± SD. Data points show the individual values, the central line represents the median, and the error bars indicate the range. Statistical analysis: two-tailed *t*-test. Source data are provided as a Source Data file.

and the bacterial membrane lipid bilayer induced rapid membrane depolarization and increased permeability, resulting in the collapse of ion gradients and the leakage of intracellular ATP and other metabolites; secondly, its cationic residues (D-arginine, D-lysine) can bind to negatively charged bacterial DNA, disrupting nucleic acid metabolism and inducing ROS bursts, further compromising bacterial homeostasis. The synergistic effect of membrane-targeting and non-membrane actions significantly elevated the genetic threshold for bacteria to escape through a single mechanism, thereby delaying the onset of drug resistance (Figs. 4 and 5).

https://doi.org/10.1038/s41467-025-65449-w

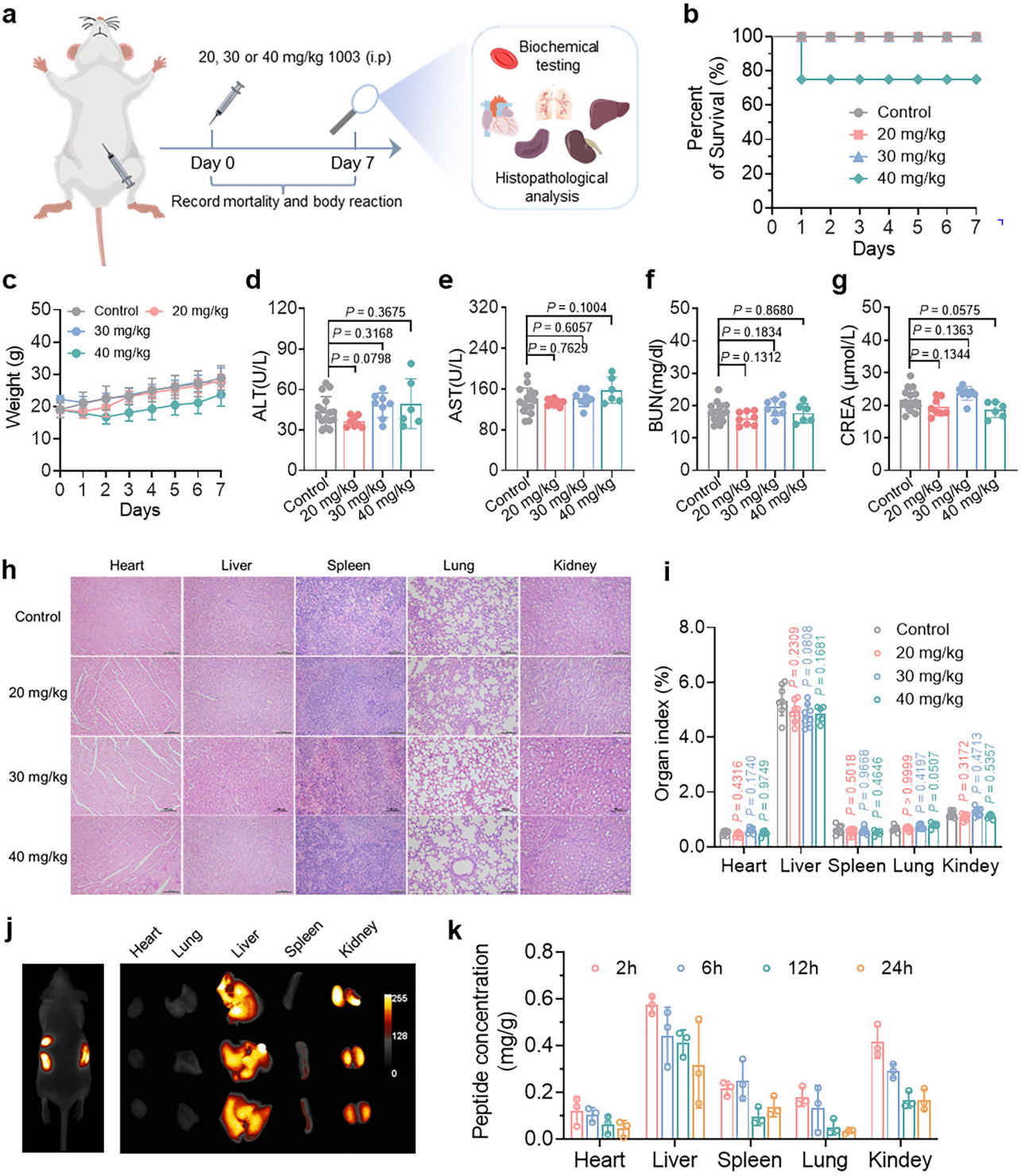

Fig. 10 | AMP 1003 showing low toxicity in vivo. a Flowchart of acute toxicity in vivo of AMP 1003. **b** Survival curves of mice treated with a single intraperitoneal injection of AMP 1003 at dose of 20 mg/kg, 30 mg/kg or 40 mg/kg. $n = 8$ mice per group. **c** The weight changes of mice administered with AMP 1003 at a dose of 20 mg/kg, 30 mg/kg or 40 mg/kg for 7 days. $n = 8$ mice for control, 20 mg/kg and 30 mg/kg group, $n = 6$ mice for 40 mg/kg group. Data are presented as mean values ± SD. Data points show the median, and the error bars indicate the range. Blood biochemical analysis (ALT (**d**), AST (**e**), BUN (**f**), CREA (**g**)) of mice at 7 days post-treatment with AMP 1003 at a dose of 20 mg/kg, 30 mg/kg or 40 mg/kg. $n = 16$ mice for control group, $n = 8$ mice for 20 mg/kg and 30 mg/kg group, $n = 6$ mice for 40 mg/kg group. Data are presented as mean values ± SD. Data points show the individual values, the central line represents the median, and the error bars indicate the range. Statistical analysis: two-tailed *t*-test. **h** Pathological sections stained by H&E of the mice's heart, liver, spleen, lung, and kidney at 7 days post-treatment with AMP 1003 at a dose of 20 mg/kg, 30 mg/kg or 40 mg/kg. Scale bar: 100 μm. **i** Organ index of the mice at 7 days post-treatment with AMP 1003 at a dose of 20 mg/kg, 30 mg/kg or 40 mg/kg. $n = 8$ mice for control, 20 mg/kg and 30 mg/kg group, $n = 6$ mice for 40 mg/kg group. Data are presented as mean values ± SD. Data points show the individual values, the central line represents the median, and the error bars indicate the range. Statistical analysis: two-tailed *t*-test. **j** Fluorescence distribution imaging of FITC-1003 in the mice at 6 h in vivo and ex vivo. **k** Biodistribution of AMP 1003 in the mice at 2, 6, 12 or 24 h, $n = 3$ mice per group. Data are presented as mean values ± SD. Data points show the individual values, the central line represents the median, and the error bars indicate the range. Source data are provided as a Source Data file.

Transcriptomics offered a systematic perspective for analyzing the multifaceted antimicrobial actions of AMP 1003. In *MRSA* (Fig. 6), it induced significant upregulation of membrane repair related genes (*CwrA*) and DNA damage response genes (*SosA*) in a concentration dependent manner, inhibited glucose transport and energy metabolism pathways, which indicated its synergistic disruption of bacterial defense networks through multidimensional stress characterized by "membrane disruption, metabolic inhibition, and oxidative stress". In *K. pneumoniae* (Fig. 7), the peptide preferentially downregulated membrane permeability related genes (such as *betB*, *betA*, *betI*) and the betaine/proline transport system (*ProV*/*ProW*/*ProX*), and inhibited the expression of the oxidative stress regulator *SoxS*, further exacerbated ROS-mediated damage. This strain specific transcriptional response difference may be attributed to differences in cell wall structure between two types of bacteria: the thick peptidoglycan layer of *MRSA* may trigger stronger membrane repair compensation mechanisms, while the outer membrane LPS layer of *K. pneumoniae* is more susceptible to electrostatic interference from cationic peptides, leading to widespread inhibition of permeability related genes[57]. It was worth noting that although the gene regulation modes of the two types of bacteria are different, AMP 1003 significantly interfered with the ABC transporter protein and transmembrane transport function, suggesting that it may prevent drug resistance by disrupting the proton dynamic potential of the bacteria and inhibiting efflux pump activity[58]. For example, the downregulation of glycerol-3-phosphate dehydrogenase in *MRSA* and the inhibition of anaerobic glycerol-3-phosphate dehydrogenase *GlpC* in *K. pneumoniae* both indicated a comprehensive blockade of energy metabolism, which was consistent with the view that AMPs limit bacterial adaptive evolution through metabolic load theory[59]. In addition, although the downregulation of *SoxS* (*K. pneumoniae*) and the upregulation of *Hsp20* family genes (*MRSA*) may seem contradictory, they jointly reflected the stress compensation limit of bacteria in response to AMP 1003 multi-target attacks: the former accelerated ROS mediated death by weakening oxidative defense ability, while the latter temporarily enhanced protein homeostasis regulation, but ultimately led to cell collapse due to energy resource depletion[60].

Given the complexity of the host environment and the inherent toxicity of some AMPs, the clinical application of AMPs frequently encounters the challenge of inconsistent in vitro and in vivo activity[28]. Our AMP 1003, which was developed through a rational design strategy in this study, successfully overcame this limitation: it exhibited broad-spectrum antimicrobial activity and rapid bactericidal kinetics against multidrug-resistant bacteria in vitro, in addition to achieving a bacterial load reduction in a mouse infection model with low toxicity (Fig. 8). Notably, although the in vitro MICs of polymyxin B against *K. pneumoniae* and vancomycin against *MRSA* were slightly lower than that of AMP 1003 (Fig. 1d), there was no significant difference in efficacy between the two in vivo. Although in vitro assays show lower cytotoxicity for polymyxin B compared to AMP 1003 (Fig. 1i and Supplementary Fig. 8), in vivo studies indicate the opposite: AMP 1003 appears safer in mouse models (Fig. 10 and Supplementary Figs. 25–30). Polymyxin B, as the last line antibiotic against gram-negative bacterial infections, is constrained by severe nephrotoxicity due to its accumulation in the kidneys and reabsorption in the renal tubules[22]. Drugs often metabolize into less toxic or inactive forms in the body via liver enzymes like CYP3A4 or hydrolytic enzymes. For example, paclitaxel is highly toxic in vitro but is quickly metabolized by CYP3A4 in vivo, reducing toxicity[61]. Some antibiotics, such as quinolones, show lower toxicity in vivo due to rapid excretion, despite damaging eukaryotic mitochondrial DNA and inhibiting proliferation at high concentrations in vitro[62]. However, polymyxin B undergoes minimal hepatic metabolism, instead accumulates in the kidneys through tubular reabsorption, leading to sustained exposure and enhanced toxicity[63,64]. Moreover, the nephrotoxicity of polymyxin B results from mitochondrial and lysosomal damage, which is challenging to repair quickly in vivo due to the slow regeneration of renal epithelial cells[65]. Besides, animals possess protective mechanisms-such as antioxidant systems neutralizing drug-induced ROS, DNA repair enzymes fixing damage from alkylating agents, and regenerative capacities, which may reduce the toxicity of drugs like AMP 1003. For instance, acetaminophen is highly toxic to liver cells in vitro but can be detoxified in animals with N-acetylcysteine[66].

The inflammatory response triggered by bacterial infection serves as a crucial defense mechanism enabling hosts to resist pathogen invasion. Moreover, it represents a complex pathological process involving interactions between the immune system and microorganisms[54]. When bacteria invade the body via respiratory or digestive pathways, their pathogen-associated molecular patterns, such as LPS and peptidoglycans, are specifically recognized by host pattern recognition receptors. This recognition activates innate immune cells, such as macrophages and neutrophils, and initiates inflammatory signaling pathways[67]. Consequently, this process promotes the release of pro-inflammatory mediators, resulting in typical inflammatory features, including vasodilation and immune cell infiltration[68]. However, when infection persists or immune regulation is imbalanced, excessive inflammatory response may lead to severe consequences, including tissue damage, sepsis, or multiple organ dysfunction. The continuous emergence of antibiotic-resistant bacteria has exacerbated the challenge of infection control, prompting the regulation of host inflammatory pathways as a strategy for anti-infection therapy[69]. Striking a balance between pathogen elimination and preserving immune homeostasis remains a focal point of research. This study systematically evaluated the anti-inflammatory activity of AMP 1003 based on an inflammation model induced by LPS. In RAW 264.7 cells, LPS significantly upregulated the expression of pro-inflammatory cytokines, while the release of these key inflammatory mediators was inhibited by the peptide in a dose-dependent manner (Fig. 9b–g). In the LPS-induced acute lung injury model, the peptide effectively alleviated typical pathological features observed in the lungs, including bronchial epithelial injury and alveolar hemorrhage. It also significantly reduced inflammatory markers such as *Tnf-α*, *Il-1β*, and *Mcp1* in lung tissue, thereby confirming its in vivo anti-inflammatory efficacy (Fig. 9i–n). These results corresponded to the uncontrolled inflammation related to bacterial infections and highlighted the potential therapeutic value of AMP 1003 in inhibiting cytokine storms through multiple targets. Notably, the peptide did not directly target pathogens but mitigated tissue damage by regulating the host immune response. This strategic approach may circumvent the issue of antibiotic resistance and may offer new perspectives for adjuvant therapy in sepsis and drug-resistant bacterial infections associated with inflammation.

In conclusion, AMP 1003, developed through a rational design strategy in this study, has substantially addressed the limitations associated with inadequate stability, elevated toxicity, and the induction of drug resistance characteristic of traditional AMPs. It has not only accomplished a synergistic optimization of stability, antimicrobial activity and biocompatibility, but also postponed the emergence of drug resistance through multiple mechanisms, including membrane targeting and non-membrane action. Furthermore, it has exhibited comparable efficacy and superior safety relative to polymyxin B in a mouse infection model. Nevertheless, despite the apparent translational potential of AMP 1003, several limitations remain to be addressed. Firstly, the promising therapeutic window for systemic administration has yet to be fully delineated, particularly concerning pharmacokinetic characteristics in hosts suffering from liver and kidney dysfunction or immunosuppression; these factors necessitate systematic evaluation. Secondly, the potential immunogenicity risks associated with long-term repeated administration warrant consideration. Additionally, current research primarily focuses on acute

infection models, thus requiring further investigation into the permeability and efficacy of AMP 1003 in chronic biofilm infections or deep tissues, such as bones, joints, and the central nervous system. Consequently, it is crucial to further optimize the metabolic stability and tissue targeting of AMP 1003 in future research while more accurately analyzing the key pathways involved in its mechanism of action (e.g., the SOS response and membrane repair) to facilitate the enhancement of multi-target synergistic effects and to validate the sustained efficacy of the peptide in animal models of immunodeficiency or chronic infection.

Methods

Ethics statement

Kunming mice were obtained from the Medical Experimental Animal Center of Lanzhou University (China). All mice used in this study were handled strictly according to the Guide for the Care and Use of Laboratory Animals of the National Institutes of Health. The official procedure was approved by the Ethics Committee of Lanzhou University (Permit Number: SYXK Gan 2018-0002), China. Mice were raised at 20–22 °C and 40–70% humidity, with a dark-light cycle of 12 h.

Bacterial strains

The standard bacterial strains *MRSA* ATCC 33591, *K. pneumoniae* ATCC 700603, *A. baumannii* ATCC 19606, *E. coli* ATCC 25922, *P. aeruginosa* ATCC 27853, *P. aeruginosa* ATCC 9027, *S. aureus* ATCC 25923, *S. aureus* ATCC 29213, *S. epidermidis* ATCC 12228, *E. faecalis* ATCC 29212 was purchased from the American Type Culture Collection (ATCC). The clinical isolates of bacterial strains *MRSA* MDR1-6, *K. pneumoniae* MDR1-5, *A. baumannii* MDR1, *E. coli* MDR1, *P. aeruginosa* MDR1, *S. aureus* MDR1, *E. faecalis* MDR1 were obtained from Culture Collection Center of School of Basic Medical Sciences of Lanzhou University (China). All bacteria were cultured in Mueller-Hinton (MH) broth medium overnight at 37 °C to mid-logarithmic phase before each experiment.

Synthesis and characterization of peptide

The peptide was synthesized via classical solid-phase methods using standard Fluorenylmethoxycarbonyl (Fmoc) chemistry on Rink amide 4-methylbenzhydrylamine (MBHA) resin (Hecheng, China)[25]. All Fmoc-amino acids (Fmoc-D-Trp(Boc)-OH, Fmoc-D-Arg(Pbf)-OH, Fmoc-D-Lys(Boc)-OH), 1-Hydroxybenzotriazole (HOBT), O-Benzotriazole-N,N,N′,N′-tetramethyl-uronium-hexafluorophosphate (HBTU) were purchased from GL Biochem (China). Initially, the resin (0.25 mmol) was swollen by bubbling in DCM (10 mL) for 30 min. The Fmoc group was removed by treatment with 20% piperidine/DMF (v/v), followed by washing with DMF. Then, the coupling reactions were carried out by treatment with a solution of Fmoc-amino acid (3 equiv), HBTU (3 equiv), HOBt (3 equiv), and DIEA (6 equiv) in DMF. After 1 h of coupling reaction, and the resin was washed with DMF to check whether the coupling is successful with ninhydrin. After completing each coupling, the Fmoc group of N-terminal was removed by treatment with 20% piperidine/DMF (v/v) and the resin was expanded (DCM) and compressed (methanol). Final cleavage was conducted with a cleavage reagent consisting of TFA/ H_2O/TIS (95:2.5:2.5, v/v/v) for 3 h at room temperature. The obtained crude peptide was purified by reverse high-performance liquid chromatography (RP-HPLC, Waters Massachusetts, USA) on a C18 column (19 mm × 250 mm) with an acetonitrile gradient in water containing 0.05% trifluoroacetic acid (v/v). Its purity was analyzed by RP-HPLC on a C18 column (4.6 mm × 250 mm) and molecular weight was determined by electrospray ionization-mass spectrometry (EI-MS, MaXis 4G, Bruker, USA). Physical and chemical parameters were predicted by ChemDraw 18.0 and Expasy-ProtParam. Circular dichroism (CD) spectrum of the peptide in H_2O or 50% TFE was analyzed using a J-810 spectrometer (Jasco, Japan) with a wavelength detection range spanning from 190 nm to 250 nm and an optical path length of 1 mm.

Minimum inhibitory concentration (MIC) assay

The in vitro antimicrobial activity of the peptide or antibiotic was evaluated using the classic double microdilution method, represented by MIC, according to the Clinical and Laboratory Standards Institute[47]. The mid-logarithmic phase of bacteria was diluted to 1×10^6 CFU/mL in MH broth medium and mixed with equal volumes of peptide or antibiotic solutions diluted using the double dilution method. After incubation at 37 °C for 18 h, the MIC was defined as the lowest concentration of the peptide or antibiotic at which no visible bacterial growth occurred.

Bacterial killing kinetics

The mid-logarithmic phase of bacteria was diluted to 1×10^6 CFU/mL, which was mixed with different concentrations of peptide or antibiotic solutions in equal volumes and incubated at 37 °C. At different time points, equal portions of the co-incubation were diluted and coated onto MH agar plates, and the plates were incubated at 37 °C for 18 h for bacterial counting.

Biocompatibility assay

Hemolysis assay. Fresh mouse erythrocytes were collected and washed with PBS to prepare a suspension containing 8% (v/v) red blood cells. The red blood cell suspensions were exposed to different concentrations of peptide solutions at 37 °C for 1 h. After centrifugation at 1200 × *g* at 4 °C for 15 min, the absorbance of supernatant at 490 nm was recorded using a microplate reader (Flex Station 3, USA). Untreated erythrocytes were used as a negative control and erythrocytes treated with 1% Triton X-100 were employed as a positive control. The hemolysis rate was calculated: Hemolysis (%) = $[(OD_{490\,nm\ (peptides)} - OD_{490\,nm\ (negative\ control)}) / (OD_{490\,nm\ (positive\ control)} - OD_{490\,nm\ (negative\ control)})] \times 100\%$.

Cytotoxicity assay. MTT assay was performed to evaluate the cytotoxicity of the peptide against BV-2 cells, RAW 264.7 cells and HK-2 cells. Cells were cultured in DMEM medium containing 10% FBS and plated in a 96-well plate at a cell density of 6000 cells/well for 24 h at 37 °C in 5% CO_2. The different concentrations of peptide solutions were added to the 96-well plate to further incubate for 24 h. MTT (5 mg/mL) solution was added to each well, followed by an extra 4 h of incubation in the dark. After that, the supernatant was carefully discarded and dimethyl sulfoxide was used to fully solubilize the formazan crystals, of which a microplate reader detected the absorbance at 570 nm. At the same time, SYTO-9/PI (Invitrogen, USA) was used to visually analyze cytotoxicity by a confocal laser scanning microscope (Zeiss LSM 710 Meta; Carl, Germany).

Stability assay

The stability of peptide in different concentrations of protease (trypsin, chymotrypsin, pepsin), salt ions (Na^+ or Mg^{2+}) and serum (mouse serum, FBS, NBCS) was measured using the above MIC determination method. Among them, protease and mouse serum need to be co-incubated with peptide for 6 h in advance and treated at 60 °C for 15 min to terminate the reaction, and then was used to determine the MIC or analyze by RP-HPLC.

Combination with antibiotics

The classic chessboard method was used to investigate the combined antimicrobial effect of peptide and antibiotics. The mid-logarithmic phase of bacteria was diluted to 1×10^6 CFU/mL and added to a 96-well plate with a pre-prepared mixture solution of peptides and antibiotics in a checkerboard pattern in equal volumes. After incubation at 37 °C for 18 h, the lowest drug concentration without visible bacterial growth

was used as the MIC of the peptide or antibiotic when combined. The FICI (fractional inhibitory concentration index) was calculated using the following formula: FICI = (MIC of peptide in combination/MIC of peptide alone) + (MIC of antibiotic in combination/MIC of antibiotic alone). Among them, FICI ≤ 0.5 indicated synergy; 0.5 < FICI ≤ 1.0 indicated additive; 1.0 < FICI < 4.0 indicated indifference; FICI ≥ 4.0 indicated antagonism.

Antimicrobial-resistance test

A continuous MIC assay was used to investigate the development of antimicrobial resistance. The MIC of peptide or antibiotics was measured using the above MIC determination method. After culturing at 37 °C for 18 h, the bacterial suspension in 1/2 × MIC was transferred to be cultivated in fresh MH broth medium for the next MIC determination. The measurement was repeated 15 times, and the changes in MIC were recorded to assess the development of antimicrobial resistance. In addition, the cross-resistance between peptide and antibiotics was evaluated using the MIC determination method.

Chemo sensitization assay

Chemo sensitization assay was used to evaluate whether the peptide can regulate the antimicrobial resistance of antibiotic[21]. Simply, the MIC of the antibiotic against resistant bacteria was determined in the presence or absence of peptide at sub-inhibitory concentrations (1/4 × MIC or 1/2 × MIC) using the MIC determination method.

Kill kinetics on bacterial persister cells

The mid-logarithmic phase of bacteria was diluted to 2×10^8 CFU/mL and exposed to the antibiotic at a concentration of 10 × MIC for 18 h at 37 °C. The co-incubation was evenly washed with PBS to remove the remaining antibiotics and then added to the peptide solutions. The suspensions were continued to culture at 37 °C, and equal portions were taken at various time points to spread on MH agar plates for bacterial counting.

Antimicrobial mechanism

LPS/LTA/PC competitive inhibition assay. Lipopolysaccharide (LPS, from *E. coli* O111:B4, Sigma-Aldrich, USA), Lipoteichoic acid (LTA, from *S. aureus*, Sigma-Aldrich, USA) or L-α-Phosphatidylcholine (PC, Sigma-Aldrich, USA) was dissolved in PBS (10 mM, pH 7.4) with different concentrations, which mixed with an equal volume of peptide to incubate at 37 °C for 1 h. Then, the co-incubation was mixed with an equal volume of bacterial suspensions (1×10^6 CFU/mL) and incubated for 18 h. The absorbance at 600 nm was measured by a microplate reader, and the bacterial survival rate was calculated to assess the binding ability of the peptide to LPS/LTA/PC.

Outer membrane permeability assay. The effect of peptide on bacterial outer membrane permeability was investigated using fluorescent dye 1-N-phenylnaphthylamine (NPN, Sigma-Aldrich, USA). The mid-logarithmic phase of bacteria was diluted to $OD_{600\ nm} = 0.5$, then suspended in HEPES buffer solution (5 mM, pH 7.4) in half volume. The different concentrations of peptide solutions were prepared in PBS and mixed with NPN dye (40 μM) in a 96-well blackboard. Next, the bacterial suspension mentioned above was added, and the fluorescence intensity (excitation wavelength of 350 nm, emission wavelength of 420 nm) was detected immediately by a microplate reader. The percentage of NPN uptake was calculated according to the following formula: NPN uptake% = $[(F_t - F_0)/(F_m - F_0)] \times 100\%$, where F_t is the NPN fluorescence intensity of the peptide group; F_0 is the NPN fluorescence intensity without peptide or bacteria; F_m is the NPN fluorescence intensity of Polymyxin B (10 μg/mL).

Cytoplasmic membrane depolarization assay. The membrane potential sensitive fluorescent probe 3,3-dipropylthiadicarbocyanine iodide ($DiSC_3$-5, Sigma-Aldrich, USA) was used to investigate the cytoplasmic membrane depolarization ability of peptide. The mid-logarithmic phase of bacteria was diluted to $OD_{600\ nm} = 0.1$ in HEPES buffer (5 mM, pH 7.4, containing 20 mM glucose and 0.1 M KCl) and incubated with $DiSC_3$-5 (4 μM) at 37 °C until fluorescence stabilizes. Then, the co-incubation was added to a black 96-well plate with different concentrations of peptide solutions, and the fluorescence intensity (excitation wavelength of 622 nm, emission wavelength of 670 nm) was recorded by a microplate reader.

Membrane integrity assay. Bacterial membrane integrity was evaluated by propidium iodide (PI, Sigma-Aldrich, USA) dye. Bacterial suspension (10×10^8 CFU/mL) was incubated with peptide solutions for 2 h at 37 °C, and then stained with PI dye (1 mg/mL) for 15 min. The fluorescence intensity (excitation wavelength = 535 nm, emission wavelength = 615 nm) was recorded by a microplate reader.

Confocal laser scanning microscope characterization. The mid-logarithmic phase of bacteria was diluted to 10×10^8 CFU/mL and mixed with peptide solutions for 2 h at 37 °C, followed by a 30 min incubation with SYTO-9/PI (Invitrogen, USA) dye. The images were obtained by a confocal laser scanning microscope (Zeiss LSM 710 Meta; Carl Zeiss, Germany) and analyzed by ZEN Light Edition software (Zeiss, Germany).

Scanning electron microscope (SEM) characterization. SEM was used to characterize the bacterial membrane morphology. The mid-logarithmic phase of bacteria was diluted to 10×10^8 CFU/mL and incubated with peptide solutions for 2 h at 37 °C. Subsequently, the mixture was fixed with 3% (w/v) glutaraldehyde at 4 °C overnight and washed with PBS, then continuously treated with a graded ethanol series (50%, 70%, 80%, 90%, and 100%) for 10 min and tertbutanol for 2 h. The final samples were dried and coated with gold to capture the images using Apreo S (Thermo fisher Scientific, MA, USA).

DNA gel retardation assay. DNA gel retardation test was carried out to measure the affinity of peptide to the bacterial genomic DNA. The genomic DNA of bacteria was extracted using the TIANamp Bacteria DNA Kit (TIANGEN, China) and incubated with different concentrations of peptide solutions at 37 °C for 30 min. The samples were used to conduct electrophoresis using 1% agarose gels, and the migration of DNA was detected by the fluorescence of Gel-Red using an Image Quant 300 gel documentation system (GE Healthcare, USA). The presentation of full scan gels was presented in the Source Data file.

ROS accumulation assay. The ROS accumulation of bacteria exposed to peptide was measured by 2′,7′-dichloroffuorescein diacetate (DCFH-DA, Beyotime, China) probe[44]. The mid-logarithmic phase of bacteria was diluted to $OD_{600\ nm} = 0.5$ in PBS, and then incubated with different concentrations of peptide solutions in a 96-well black plate. Subsequently, DCFH-DA (100 μM) was quickly seeded into and the fluorescence (excitation wavelength = 488 nm, emission wavelength = 525 nm) was recorded by a microplate reader. Antioxidant NAC was a negative control.

Nucleic acid and protein leakage. The mid-logarithmic phase of bacteria was suspended in PBS at a bacterial density of 10×10^8 CFU/mL, and incubated with different concentrations of peptide solutions at 37 °C. At different time points, aliquots of co-incubation were taken and centrifuged to measure the absorbance of supernatant at 260 nm and 280 nm using a microplate reader.

Extracellular and intracellular ATP. Extracellular and intracellular ATP levels of bacteria exposed to peptide were detected by an ATP Assay Kit (Beyotime, China). In brief, the mid-logarithmic phase of

bacteria was diluted to OD_{600} nm = 0.5 in PBS and incubated with different concentrations of peptide solutions for 60 min. After centrifugation at 12,000 × *g* for 5 min at 4 °C, the supernatant was collected to determine the extracellular ATP level, and the bacterial precipitates were lysed using lysozyme to detect the intracellular ATP.

Transcriptome analysis of *MRSA* or *K. pneumoniae* treated with peptide

Bacteria were grown overnight in MH broth, diluted to 10×10^8 CFU/mL with peptide (4 × MIC or 2 × MIC), and incubated for 2 h. Then the bacteria were washed with fresh PBS and the bacterial cells were spun down by centrifuging at 8000 × *g* for 10 min at 4 °C. Total RNA was extracted using the RNAprep pure Cell/Bacteria Kit (TIANGEN, China). RNA purity and quantification were evaluated using the NanoDrop 2000 spectrophotometer (Thermo Scientific, USA). RNA integrity was assessed using the Agilent 2100 Bioanalyzer (Agilent Technologies, USA). The samples with qualified purity, quantity and integrity were utilized for subsequent library construction. TIANSeq rRNA Depletion Kit (TIANGEN, China) was used to remove ribosomal RNA, then the libraries were constructed using VAHTS Universal V6 RNA-seq Library Prep Kit according to the manufacturer's instructions. The transcriptome sequencing was conducted by OE Biotech Co., Ltd (Shanghai, China). Using the estimate Size Factors function of the R package of DESeq2 to standardize counts, and use the nbinom-test function to calculate the *p*-value and Fold change of the difference comparison. The DEGs were analyzed by the DESeq2 package using a |Fold change| ≥ 2 and adjusted *p*-value < 0.05, and hypergeometric distribution tests were performed to determine the GO and KEGG enrichment analysis of the DEGs to determine the biological functions or pathways that were mainly affected by differential genes. Each group underwent three separate experiments.

Bacteria-induced pneumonia model

The in vivo antimicrobial activity of the peptide was assessed by the pneumonia model. Male Kunming mice (weighing 20 ± 2 g, 6–8 weeks old) were induced neutropenia by injection *i.p.* with two doses of cyclophosphamide on day 1 (150 mg/kg) and day 4 (100 mg/kg). On day 5, mice were *i.p.* administered pentobarbital at a dose of 60 mg/kg and infected by injecting *MRSA* ATCC 33591 (25 μL, 1×10^9 CFU/mL) or *K. pneumoniae* ATCC 700603 (25 μL, 1×10^9 CFU/mL) via intratracheal spraying. Mice were randomly assigned to four groups (6 per group). They were injected *i.p.* with peptide or vancomycin (for *MRSA* ATCC 33591 infection) or polymyxin B (for *K. pneumoniae* ATCC 700603 infection) at a single dose of 5 or 10 mg/kg at 4 h, 8 h and 12 h post-infection, respectively. The model group was injected with the same volume of normal saline. After 24 h post-infection, the mice were euthanized, and the lung was taken out for bacterial counting and histopathological examination.

Reverse transcription quantitative real-time PCR (RT-qPCR)

RAW 264.7 cells were cultured in DMEM medium containing 10% FBS and seeded in a 12-well plate with a cell density of 1×10^5 cells/well for 24 h at 37 °C in 5% CO_2, then exposed to LPS from *E. coli* O111: B4 (1 μg/mL) for 1 h. Following incubation with peptide solutions for 2 h, total RNA of RAW 264.7 cells was isolated and analyzed. Total RNA was extracted with TRNzol isolation reagent (TIANGEN, China) and reverse-transcribed to cDNA using a high-capacity reverse transcription kit. The target mRNA amount in the samples was detected using SYBR-Green, and the relative mRNA expression levels of various genes were determined by quantitative RT-qPCR on the QuantStudio 3 Instrument (Applied Biosystems, USA). Normalized to the mRNA expression level of *β-actin*, the mRNA expression of other genes was calculated using the $2^{-\Delta\Delta Ct}$ method. All primers used in this study were designed for this project using the NCBI Primer-BLAST tool and were synthesized by Sangon Biotech (Shanghai, China). The paired primers used for amplification are listed in Supplementary Table 1.

LPS-induced acute lung injury model

Male Kunming mice (weighing 20 ± 2 g, 6–8 weeks old) were induced to neutropenia by injection *i.p.* with two doses of cyclophosphamide on day 1 (150 mg/kg) and day 4 (100 mg/kg). On day 5, mice were *i.p.* administered pentobarbital at a dose of 60 mg/kg and modeled by injecting LPS from *E. coli* O111: B4 (5 mg/kg) via intratracheal spraying. Mice were randomly assigned into three groups (6 per group) and injected *i.p.* with the peptide at a single dose of 5 mg/kg at 2, 6 and 10 h post molding, respectively. The model group was injected with the same volume of saline. After 12 h post molding, the mice were euthanized and the lung was taken out for extracting total RNA to analyze by RT-qPCR and for histopathological examination.

In vivo toxicity assay

The in vivo toxicity of the peptide was tested by a single intraperitoneal injection in mice. Specifically, Kunming mice (weighing 20 ± 2 g, 6–8 weeks old, randomly allocated 4 male mice and 4 female mice to each group) were *i.p.* injected with the peptide or polymyxin B at a single dose of 20, 30 or 40 mg/kg. Saline was employed as the control group. Behavior, weight and survival of mice were recorded for 7 days or until death. Additionally, mice were sacrificed after 7 days post administration, serum and urine were collected for biochemical and protein expression analysis, and organs were harvested for histopathological examination and transcriptome analysis. Renal tubular injury score was estimated in renal tissue stained with hematoxylin and eosin[70]. Renal tubular injury is classified into six levels based on brush border loss, tubular dilation, cast formation, tubular necrosis, and neutrophil filtration. Ten high-power fields were chosen randomly, with scores ranging from 0 to 5 for each field (0: normal; 1: mild injury, affected 0–10%; 2: moderate injury, affected 11–25%; 3: severe injury, affected 26–49%; 4: highly severe injury, affected 50–75%; 5: extensive injury, affected 75%). All evaluations were conducted by two researchers who had no knowledge of the experimental conditions.

Enzyme-linked immunosorbent assay (ELISA)

The ELISA kits used to detect the levels of mouse neutrophil gelatinase-associated lipocalin (NGAL) (JX-3003A1, Yancheng Junxing Biotechnology Co., Ltd, China), Cystatin C (JX-3175A1, Yancheng Junxing Biotechnology Co., Ltd, China) and kidney injury molecule-1 (Kim-1) (JX-3054A1, Yancheng Junxing Biotechnology Co., Ltd, China) in serum and urine. The operations were conducted according to the manufacturer's instructions.

Biodistribution

Standard curve of fluorescamine assay. Peptide was dissolved in PBS to prepare a 1 mg/mL stock solution and then gradually diluted into different concentrations (0.5 mg /mL, 0.25 mg/mL, 0.125 mg/mL, etc.). Fluorescamine powder was dissolved in DMSO to prepare a 3 mg/mL working reagent. In a 384-well black plate, 27 μL of peptide solutions at different concentrations were mixed with 9 μL of fluorescamine working reagent. After incubating for 15 min in the dark, the fluorescence intensity (excitation wavelength at 395 nm and emission wavelength at 470 nm) was recorded by a microplate reader. A standard curve was obtained based on the concentration of the peptide solution and its corresponding fluorescence intensity.

Biodistribution. Male Kunming mice (weighing 20 ± 2 g, 6–8 weeks old) were randomly assigned to four groups (*n* = 3 mice per group) and intravenously injected with peptide (5 mg/kg, 100 μL). At 2, 6, 12, and 24 h, the organs were collected and homogenized in PBS. After centrifugation at 10,000 × *g* for 10 min, the supernatant was collected. In a

384-well black plate, the supernatants (27 μL) were mixed with the fluorescamine working reagent (9 μL, 3 mg/mL) and incubated in the dark for 15 min. The fluorescence intensity was tested by a microplate reader using the excitation wavelength at 395 nm and the emission wavelength at 470 nm. The amount of peptide at different time points was calculated using a standard curve (Supplementary Fig. 3l). Additionally, peptide was marked by FITC and the distribution of fluorescence was then observed by a small animal live imaging system (Bio-Rad ChemiDoc MP, Times-Legend Bioscientific Co., LTD) at 6 h after intravenous injection with FITC-peptide, respectively. Finally, the mice were humanely executed and the organs were ex vivo imaged immediately after in vivo imaging at 6 h.

Statistical analyses

Data normality was tested by the Shapiro-Wilk test and graphically by QQ plot (R). Data were expressed as mean ± standard deviation (SD) and statistically analyzed by GraphPad Prism version 9.0 (Chicago, IL, USA). Student's *t* test (two-tailed) was used to determine significance between the two groups. Exact *p* values are shown on the graph.

Reporting summary

Further information on research design is available in the Nature Portfolio Reporting Summary linked to this article.

Data availability

The transcriptomic dataset of strains generated in this study is available on the National Center for Biotechnology Information (NCBI) database with SRA accession code: PRJNA1224220. All data generated in this study are provided in the Supplementary Information/Source Data file. Source data are provided with this paper.

References

1. Schonrich, G. & Raftery, M. J. CD1-restricted T cells during persistent virus infections: "Sympathy for the Devil". *Front. Immunol.* **9**, 545 (2018).
2. de Benedictis, F. M. et al. Complicated pneumonia in children. *Lancet* **396**, 786–798 (2020).
3. Tong, S. Y., Davis, J. S., Eichenberger, E., Holland, T. L. & Fowler, V. G. Jr Staphylococcus aureus infections: epidemiology, pathophysiology, clinical manifestations, and management. *Clin. Microbiol. Rev.* **28**, 603–661 (2015).
4. de Breij, A. et al. The antimicrobial peptide SAAP-148 combats drug-resistant bacteria and biofilms. *Sci. Transl. Med.* **10**, eaan4044 (2018).
5. Hui, J. et al. Photo-disassembly of membrane microdomains revives conventional antibiotics against MRSA. *Adv. Sci.* **7**, 1903117 (2020).
6. Enright, M. C. et al. The evolutionary history of methicillin-resistant Staphylococcus aureus (MRSA). *Proc. Natl. Acad. Sci. USA* **99**, 7687–7692 (2002).
7. Harkins, C. P. et al. Methicillin-resistant Staphylococcus aureus emerged long before the introduction of methicillin into clinical practice. *Genome Biol.* **18**, 130 (2017).
8. Yang, X., Dong, N., Chan, E. W., Zhang, R. & Chen, S. Carbapenem resistance-encoding and virulence-encoding conjugative plasmids in Klebsiella pneumoniae. *Trends Microbiol.* **29**, 65–83 (2021).
9. Paczosa, M. K. & Mecsas, J. Klebsiella pneumoniae: going on the offense with a strong defense. *Microbiol. Mol. Biol. Rev.* **80**, 629–661 (2016).
10. Russo, T. A. et al. Differentiation of hypervirulent and classical Klebsiella pneumoniae with acquired drug resistance. *mBio*. **15**, e0286723 (2024).
11. Russo, T. A. et al. Identification of biomarkers for differentiation of hypervirulent Klebsiella pneumoniae from classical K. pneumoniae. *J. Clin. Microbiol.* **56**, e00776-18 (2018).
12. Tacconelli, E. et al. Discovery, research, and development of new antibiotics: the WHO priority list of antibiotic-resistant bacteria and tuberculosis. *Lancet Infect. Dis.* **18**, 318–327 (2018).
13. *Antimicrobial Resistance Global Report on Surveillance* (World Health Organization, 2014).
14. Qin, X. et al. Antimicrobial resistance of clinical bacterial isolates in China: current status and trends. *JAC Antimicrob. Resist.* **6**, dlae052 (2024).
15. Tian, L. et al. Epidemiology of Klebsiella pneumoniae bloodstream infections in a teaching hospital: factors related to the carbapenem resistance and patient mortality. *Antimicrob. Resist. Infect. Control* **5**, 48 (2016).
16. Hancock, R. E. & Sahl, H. G. Antimicrobial and host-defense peptides as new anti-infective therapeutic strategies. *Nat. Biotechnol.* **24**, 1551–1557 (2006).
17. Mookherjee, N., Anderson, M. A., Haagsman, H. P. & Davidson, D. J. Antimicrobial host defence peptides: functions and clinical potential. *Nat. Rev. Drug Discov.* **19**, 311–332 (2020).
18. Magana, M. et al. The value of antimicrobial peptides in the age of resistance. *Lancet Infect. Dis.* **20**, e216–e230 (2020).
19. Lazzaro, B. P., Zasloff, M. & Rolff, J. Antimicrobial peptides: application informed by evolution. *Science* **368**, eaau5480 (2020).
20. Teixeira, V., Feio, M. J. & Bastos, M. Role of lipids in the interaction of antimicrobial peptides with membranes. *Prog. Lipid Res.* **51**, 149–177 (2012).
21. Zhong, C. et al. Antimicrobial peptides with symmetric structures against multidrug-resistant bacteria while alleviating antimicrobial resistance. *Biochem. Pharm.* **186**, 114470 (2021).
22. Falagas, M. E. & Kasiakou, S. K. Toxicity of polymyxins: a systematic review of the evidence from old and recent studies. *Crit. Care* **10**, R27 (2006).
23. Li, X. et al. Peptide double-stapling and arginine N-glycosylation triggered the development of therapeutic antimicrobial peptides capable of killing drug-resistant bacteria in mice. *J. Med. Chem.* **68**, 4511–4526 (2025).
24. Ong, Z. Y., Wiradharma, N. & Yang, Y. Y. Strategies employed in the design and optimization of synthetic antimicrobial peptide amphiphiles with enhanced therapeutic potentials. *Adv. Drug Deliv. Rev.* **78**, 28–45 (2014).
25. Zhong, C. et al. Design and synthesis of new N-terminal fatty acid modified-antimicrobial peptide analogues with potent in vitro biological activity. *Eur. J. Med. Chem.* **182**, 111636 (2019).
26. Pandi, A. et al. Cell-free biosynthesis combined with deep learning accelerates de novo-development of antimicrobial peptides. *Nat. Commun.* **14**, 7197 (2023).
27. Liu, H. et al. De novo design of self-assembling peptides with antimicrobial activity guided by deep learning. *Nat. Mater.* **24**, 1295–1306 (2025).
28. Fjell, C. D., Hiss, J. A., Hancock, R. E. & Schneider, G. Designing antimicrobial peptides: form follows function. *Nat. Rev. Drug Discov.* **11**, 37–51 (2011).
29. Bui Thi Phuong, H., Doan Ngan, H., Le Huy, B., Vu Dinh, H. & Luong Xuan, H. The amphipathic design in helical antimicrobial peptides. *ChemMedChem*. **19**, e202300480 (2024).
30. Shao, C. et al. Central beta-turn increases the cell selectivity of imperfectly amphipathic alpha-helical peptides. *Acta Biomater.* **69**, 243–255 (2018).
31. Arias, M., Piga, K. B., Hyndman, M. E. & Vogel, H. J. Improving the activity of Trp-rich antimicrobial peptides by Arg/Lys substitutions and changing the length of cationic residues. *Biomolecules* **8**, 19 (2018).
32. Zhong, C. et al. New antimicrobial peptides with repeating unit against multidrug-resistant bacteria. *ACS Infect. Dis.* **7**, 1619–1637 (2021).

33. Lu, J. et al. D- and unnatural amino acid substituted antimicrobial peptides with improved proteolytic resistance and their proteolytic degradation characteristics. *Front. Microbiol.* **11**, 563030 (2020).
34. Xiong, M. et al. Helical antimicrobial polypeptides with radial amphiphilicity. *Proc. Natl. Acad. Sci. USA* **112**, 13155–13160 (2015).
35. Zheng, Y. et al. Imidazole-rich, four-armed host-defense peptidomimetics as promising narrow-spectrum antibacterial agents and adjuvants against pseudomonas aeruginosa infections. *Adv. Health. Mater.* **13**, e2400664 (2024).
36. Nguyen, L. T. et al. Serum stabilities of short tryptophan- and arginine-rich antimicrobial peptide analogs. *PLoS ONE* **5**, e12684 (2010).
37. Svenson, J., Brandsdal, B. O., Stensen, W. & Svendsen, J. S. Albumin binding of short cationic antimicrobial micropeptides and its influence on the in vitro bactericidal effect. *J. Med. Chem.* **50**, 3334–3339 (2007).
38. Liu, Y. et al. Metformin restores tetracyclines susceptibility against multidrug resistant bacteria. *Adv. Sci.* **7**, 1902227 (2020).
39. Zasloff, M. Antimicrobial peptides of multicellular organisms. *Nature* **415**, 389–395 (2002).
40. Si, Z. et al. A glycosylated cationic block poly(beta-peptide) reverses intrinsic antibiotic resistance in all ESKAPE gram-negative bacteria. *Angew. Chem. Int. Ed. Engl.* **59**, 6819–6826 (2020).
41. Fisher, R. A., Gollan, B. & Helaine, S. Persistent bacterial infections and persister cells. *Nat. Rev. Microbiol.* **15**, 453–464 (2017).
42. Jenssen, H., Hamill, P. & Hancock, R. E. Peptide antimicrobial agents. *Clin. Microbiol. Rev.* **19**, 491–511 (2006).
43. Li, B. et al. Novel beta-hairpin antimicrobial peptide containing the beta-turn sequence of -NG- and the tryptophan zippers facilitate self-assembly into nanofibers, exhibiting excellent antimicrobial performance. *J. Med. Chem.* **67**, 6365–6383 (2024).
44. Zhong, C. et al. Ultra-short lipopeptides against gram-positive bacteria while alleviating antimicrobial resistance. *Eur. J. Med. Chem.* **212**, 113138 (2021).
45. Hong, Y., Zeng, J., Wang, X., Drlica, K. & Zhao, X. Post-stress bacterial cell death mediated by reactive oxygen species. *Proc. Natl. Acad. Sci. USA* **116**, 10064–10071 (2019).
46. Dong, P. T. et al. Photolysis of staphyloxanthin in methicillin-resistant Staphylococcus aureus potentiates killing by reactive oxygen species. *Adv. Sci.* **6**, 1900030 (2019).
47. Zhang, F. et al. Short, mirror-symmetric antimicrobial peptides centered on "RRR" have broad-spectrum antibacterial activity with low drug resistance and toxicity. *Acta Biomater.* **154**, 145–167 (2022).
48. Han, W. et al. The roles of cell wall inhibition responsive protein CwrA in the pathogenicity of Staphylococcus aureus. *Virulence* **15**, 2411540 (2024).
49. Flores-Diaz, M., Monturiol-Gross, L., Naylor, C., Alape-Giron, A. & Flieger, A. Bacterial sphingomyelinases and phospholipases as virulence factors. *Microbiol. Mol. Biol. Rev.* **80**, 597–628 (2016).
50. Lv, B. et al. Heat shock potentiates aminoglycosides against gram-negative bacteria by enhancing antibiotic uptake, protein aggregation, and ROS. *Proc. Natl. Acad. Sci. USA* **120**, e2217254120 (2023).
51. Song, M. et al. A broad-spectrum antibiotic adjuvant reverses multidrug-resistant Gram-negative pathogens. *Nat. Microbiol.* **5**, 1040–1050 (2020).
52. Chen, C. et al. Structure-based mutational studies of substrate inhibition of betaine aldehyde dehydrogenase BetB from Staphylococcus aureus. *Appl. Environ. Microbiol.* **80**, 3992–4002 (2014).
53. Dietrich, L. E., Teal, T. K., Price-Whelan, A. & Newman, D. K. Redox-active antibiotics control gene expression and community behavior in divergent bacteria. *Science* **321**, 1203–1206 (2008).
54. Medzhitov, R. Origin and physiological roles of inflammation. *Nature* **454**, 428–435 (2008).
55. Srinivas, P. & Rivard, K. Polymyxin resistance in gram-negative pathogens. *Curr. Infect. Dis. Rep.* **19**, 38 (2017).
56. Brauner, A., Fridman, O., Gefen, O. & Balaban, N. Q. Distinguishing between resistance, tolerance and persistence to antibiotic treatment. *Nat. Rev. Microbiol.* **14**, 320–330 (2016).
57. Sun, J., Rutherford, S. T., Silhavy, T. J. & Huang, K. C. Physical properties of the bacterial outer membrane. *Nat. Rev. Microbiol.* **20**, 236–248 (2022).
58. Piddock, L. J. Multidrug-resistance efflux pumps—not just for resistance. *Nat. Rev. Microbiol.* **4**, 629–636 (2006).
59. Blair, J. M., Webber, M. A., Baylay, A. J., Ogbolu, D. O. & Piddock, L. J. Molecular mechanisms of antibiotic resistance. *Nat. Rev. Microbiol.* **13**, 42–51 (2015).
60. Kohanski, M. A., Dwyer, D. J., Hayete, B., Lawrence, C. A. & Collins, J. J. A common mechanism of cellular death induced by bactericidal antibiotics. *Cell* **130**, 797–810 (2007).
61. Yue, D. & Hirao, H. Mechanism of selective aromatic hydroxylation in the metabolic transformation of paclitaxel catalyzed by human CYP3A4. *J. Chem. Inf. Model* **63**, 7826–7836 (2023).
62. Kalghatgi, S. et al. Bactericidal antibiotics induce mitochondrial dysfunction and oxidative damage in Mammalian cells. *Sci. Transl. Med.* **5**, 192ra185 (2013).
63. Azad, M. A. et al. Polymyxin B induces apoptosis in kidney proximal tubular cells. *Antimicrob. Agents Chemother.* **57**, 4329–4335 (2013).
64. Sandri, A. M. et al. Population pharmacokinetics of intravenous polymyxin B in critically ill patients: implications for selection of dosage regimens. *Clin. Infect. Dis.* **57**, 524–531 (2013).
65. Dai, C., Li, J., Tang, S., Li, J. & Xiao, X. Colistin-induced nephrotoxicity in mice involves the mitochondrial, death receptor, and endoplasmic reticulum pathways. *Antimicrob. Agents Chemother.* **58**, 4075–4085 (2014).
66. Khayyat, A., Tobwala, S., Hart, M. & Ercal, N. N-acetylcysteine amide, a promising antidote for acetaminophen toxicity. *Toxicol. Lett.* **241**, 133–142 (2016).
67. Akira, S., Uematsu, S. & Takeuchi, O. Pathogen recognition and innate immunity. *Cell* **124**, 783–801 (2006).
68. Klein, S. L. & Flanagan, K. L. Sex differences in immune responses. *Nat. Rev. Immunol.* **16**, 626–638 (2016).
69. Kaufmann, S. H. E., Dorhoi, A., Hotchkiss, R. S. & Bartenschlager, R. Host-directed therapies for bacterial and viral infections. *Nat. Rev. Drug Discov.* **17**, 35–56 (2018).
70. Yang, B. et al. Caspase-3 is a pivotal regulator of microvascular rarefaction and renal fibrosis after ischemia-reperfusion injury. *J. Am. Soc. Nephrol.* **29**, 1900–1916 (2018).

Acknowledgements

The authors are grateful for the financial support from the CAMS Innovation Fund for Medical Sciences (CIFMS) (2019-I2M-5-074 (J.N.), 2021-I2M-3-001 (J.N.), 2021-I2M-1-026 (J.N.) and 2022-I2M-2-002 (J.N.)), the Program for Chang-Jiang Scholars and Innovative Research Team in University (IRT_15R27 (J.N.)), the National Natural Science Foundation of China (82404410 (C.Z.), 82173678 (J.N.) and 81773564 (J.N.)) and the talent introduction scientific research startup funds of Lanzhou University (561120208 (C.Z.)).

Author contributions

J.N., C.Z. and Y.H. conceived the idea, proposed the strategy and designed the study. J.N. supervised the study. C.Z. performed the in vitro experiments and evaluated the data. Y.H. and J.Z. (Jing Zou) contributed to the in vivo animal experiments. L.G. and J.W. synthesized the peptide. W.X. and J.Z. (Jingyi Zhu) contributed to the cytotoxicity assay. S.G., Y.Z., and H.L. contributed to the data analysis. Y.H. analyzed the transcriptomic data. J.N., C.Z. and Y.H. wrote the manuscript with input from all authors. All authors approved the final version.

Competing interests

The authors declare no competing interests.

Additional information

Supplementary information The online version contains supplementary material available at https://doi.org/10.1038/s41467-025-65449-w.

Correspondence and requests for materials should be addressed to Jingman Ni.

Peer review information *Nature Communications* thanks Francesc Rabanal, Renee Fleeman, and Seth Dickey for their contribution to the peer review of this work. A peer review file is available.

Reprints and permissions information is available at http://www.nature.com/reprints

Publisher's note Springer Nature remains neutral with regard to jurisdictional claims in published maps and institutional affiliations.

Open Access This article is licensed under a Creative Commons Attribution-NonCommercial-NoDerivatives 4.0 International License, which permits any non-commercial use, sharing, distribution and reproduction in any medium or format, as long as you give appropriate credit to the original author(s) and the source, provide a link to the Creative Commons licence, and indicate if you modified the licensed material. You do not have permission under this licence to share adapted material derived from this article or parts of it. The images or other third party material in this article are included in the article's Creative Commons licence, unless indicated otherwise in a credit line to the material. If material is not included in the article's Creative Commons licence and your intended use is not permitted by statutory regulation or exceeds the permitted use, you will need to obtain permission directly from the copyright holder. To view a copy of this licence, visit http://creativecommons.org/licenses/by-nc-nd/4.0/.

© The Author(s) 2025, modified publication 2026